Chapter – 4

Catalyzing hydrogen production: Exploring plasmonic effects in self-assembled CuO/Cu_2O thin films via pulsed laser deposition

Publication: *A. K. Ranjan, P. A. Jha, P. K. Jha, P. Singh, "Catalyzing hydrogen production: Exploring plasmonic effects in self-assembled CuO/Cu2O thin films via pulsed laser deposition" Journal of Applied Physics. 2024 May 14;135(18), p. 184902,*
https://doi.org/10.1063/5.0188802

CHAPTER 4: Catalyzing hydrogen production: Exploring plasmonic effects in self-assembled CuO/Cu_2O thin films via pulsed laser deposition

4.1 Introduction

In the previous chapter, we studied the photoconduction properties of CuO ultrathin films with Cu_2O as a defect (self-assembled). The I-V study shows that there is anisotropy in the photoconduction in all the thin films regardless of their illumination condition, which is also confirmed by theoretical studies (FEM). The study also indicates a significant current enhancement under light conditions compared to the dark, demonstrating the photoconductive nature of CuO thin films. Considering the photoconductive nature and favourable bandgap of CuO and Cu_2O, these films were used as a photocathode in the photoelectrochemical cell for hydrogen production in the present work. The escalating demand for energy and the depletion of fossil fuels underscore the urgency of transitioning to sustainable energy sources. Among these, solar energy stands out as the most abundant renewable resource, offering various pathways for electricity generation. Two notable technologies in this realm are photoelectrochemical cells (PECCs) and photoelectrolytic cells [15][132], which utilize light to drive chemical reactions. While PECCs function like photovoltaic cells, photoelectrolytic cells employ light on semiconductors or metals immersed in electrolytic solutions [15][132][133]. Notably, PECCs hold promise for hydrogen production [134][135][136] through water electrolysis, leveraging the photoelectric effect to convert electromagnetic radiation into electrical power or gas. However, challenges persist, such as multi-step reactions leading to undesirable by-products and material limitations affecting efficiency [137][138][139].

Efforts are concentrated on optimizing band alignments [140][141] and corrosion-resistant semiconductors to improve performance [142][143][144]. Fundamental to these cells is the generation of electron-hole pairs via photons with energy exceeding the bandgap. This initiates reactions at the electrode surfaces, where water oxidizes at the anode, and H^+ ions are reduced to produce H_2 gas at the cathode [144]. For these reactions, the photocathode materials should possess various features such as (a) optimum bandgap (>1.23 eV), (b) good absorption characteristics, (c) valence and conduction band edge that are distinct from the oxygen and hydrogen redox potentials, (d) corrosion resistant and stability, and (e) high conductivity and catalytic activity.

To date, research has focused on III–V systems with a bandgap of less than 2 eV, showing promising solar to hydrogen (STH) efficiencies [144][145][146][147][148]. However, concerns persist regarding their stability and high costs [145][146][147][148][149][150]. Notably, a tandem cell configuration integrating p-$GaInP_2$ with p/n-GaAs photovoltaic cells has achieved an STH efficiency of ~12.4% [146]. Furthermore, ceramic oxides such as TiO_2, WO_3, $BiVO_4$, Fe_2O_3, SnO_2, Cu_2O, and CuO are potential candidates as electrodes for water splitting in spite of their low bandgap [151][152][153] CdS, TiO_2, WS_2, $CuInS_2$, MoS_2, graphene, and their heterostructures are known for photocatalytic hydrogen production. It is reported that the formation of heterojunctions, a combination of different semiconductors, new morphology, porosity, and defect alterations influence the charge carrier lifetime and carrier mobility [47] and, hence, the reaction pathways. Bandgap engineering plays a crucial role in optimizing electronic and optical properties, influencing reaction pathways and catalytic activity. It has already been reported that bandgap engineering by structural and morphological manipulation or by doping/hybridization in C_3N_4 has influenced photoelectrochemical water splitting [154][155]. It is well known that CuO possesses desirable band alignment for H_2 production along with solar cell applications like Spiro-OMeTAD, CuH, CuI, etc. [92]. On the other hand, the CuO photocathode has shown a -4.4 mA cm^{-2} current density for the photoelectrochemical (PEC) water-splitting reaction due to enhanced charge mobility and decreased charge recombination [156].

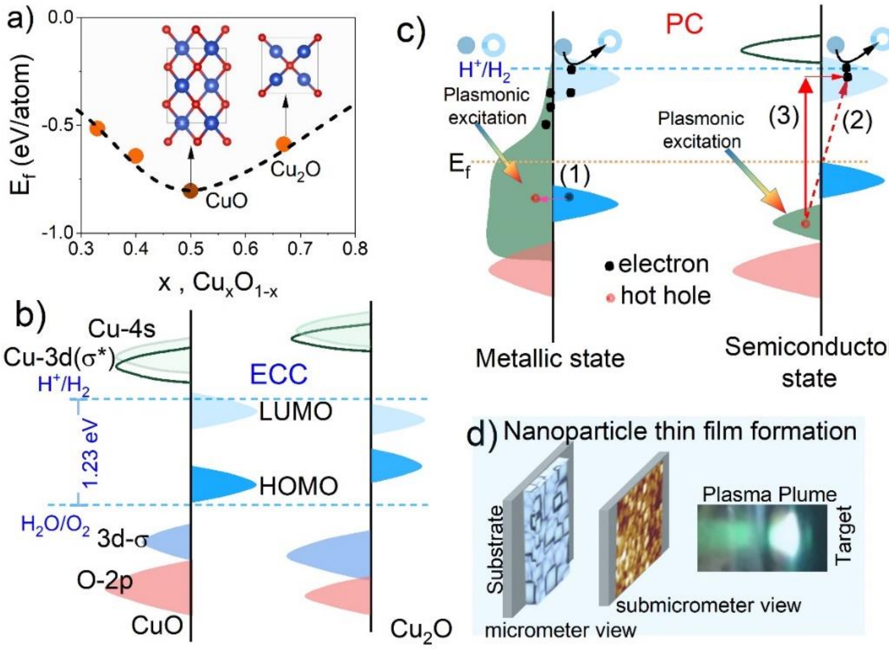

Figure 4.1: (a) Variation of formation energy of binary compounds of Cu and O showing CuO being most stable with the C2/c structure (left) and Cu_2O with the cubic phase (right). (b) Rough sketch of the band structure of CuO and Cu_2O with possible presence of adsorbates states (filled highest occupied molecular orbital (HOMO) and empty lowest unoccupied molecular orbital (LUMO) states shown in dark blue and light blue color, respectively, energy band diagram of CuO, and Cu_2O contains 4s (light green color), 3d σ* (green color), 3d σ (cyan color), and O 2p orbital (red color), during electrochemical catalysis (ECC) adsorbate state forms. (c) Illustration for the plasmonic catalysis (PC) in metallic and semiconductor states occurring via three ways, viz., (1) shows indirect hot hole transfer followed by Landau damping, (2) illustrates direct hot hole injection through adsorbates via chemical interface damping (marked by red arrows), and (3) describes indirect hot hole injection through adsorbates via chemical interface damping (marked by red arrows). Here, the kinetic energy of hot electrons transfers to adsorbates, resulting in non-thermal excitation (electron–adsorbate scattering), and then electron jumps from 3d σ (marked by green color arrows) to adsorbate state leading to 3d σ → 3d σ* transition, and the hot electrons jump from the valence band (VB) to the adsorbate state of CuO with the creation of hot hole in VB (d) illustrate the micrometer and submicrometer view of nanoparticle thin film formation using pulsed laser deposition (PLD) technique.

However, despite the desirable bandgap ~1.4 > 1.23 eV, its band alignment with redox potentials for water splitting is still a major problem concerning PECC. Meanwhile, the oxygen-deficient counterpart of CuO, i.e., Cu_2O, is being explored as solar to H_2 generation (STHG) material due to proper redox potential though its optical bandgap ~ 2.0 – 2.7 eV [91][157] is wider than 1.4 eV. Thus, the realization of bandgap widening with insight into bandgap alteration is essential for CuO, such as narrow-band materials.

Figures 4.1(a) and 4.1(b) illustrate the formation energy variation of binary Cu and O compounds, highlighting CuO's stability in the C2/c structure and Cu_2O's cubic phase. Notably, Cu_2O's formation energy exceeds that of CuO, with the nucleation size playing a crucial role in the reduction behaviour from CuO to Cu_2O [158][159][160]. This reduction behaviour may correlate with O_2 gas formation via dissociation of adsorbed O_2 and d-electron transfer [161][162]. Adsorption and desorption mechanisms significantly impact catalytic behaviour, especially in electrode contexts. The utilization of visible light in photocathodes enhances energy efficiency, with local electromagnetic fields and hot electron injection accelerating surface chemical reactions [163]. Plasmons play a key role in enhancing light absorption and catalytic reactions, particularly in plasmonic photocatalysis, where localized surface plasmon resonance (LSPR) amplifies electromagnetic fields near metal nanoparticles. This phenomenon improves light absorption and scattering, enhancing photocatalytic reactions. Non-radiative plasmonic catalysis involves various processes, including intraband (s–s, d–d) and interband (d–sp) interactions, as well as chemical interface damping, shown in Fig. 4.1(c) [164][165]. Plasmonic effects have been observed not only in metals but also in semiconductors such as tungsten oxides, copper chalcogenides, and molybdenum oxides [166], influencing charge carrier density and facilitating hot electron or hot hole transfer between semiconductor materials. For p-type plasmonic semiconductors, hot holes are generated [167], and hot hole transfer involves moving from the valence band to the highest occupied molecular orbital, followed by Landau damping, marked as (1) in Fig. 4.1(c) [167][168]. Other potential mechanisms are direct hot electron injection from the valence band (VB) to the lowest unoccupied molecular orbital (LUMO) is observed, marked as (2) in Fig. 4.1(c), alongside indirect hot hole injection, marked as (3) in Fig. 4.1(c) via molecular adsorbates referred to as chemical interface damping. Strategies such as reducing depletion layer thickness and incorporating anisotropic LSPR in semiconductor nanostructures enhance photocatalysis. The complex interplay of factors like thickness, particle size, and shape fine-tune plasmonic resonance offers opportunities for tailored optical and electronic properties. Plasmonic semiconductor materials show promise for hydrogen generation due to their strong LSPR. However, the energetic favourability of plasmonic heating for solar-to-hydrogen generation in CuO/Cu_2O systems requires further investigation. Interdisciplinary research is crucial for advancing hydrogen generation technology and understanding the role of chemical interface damping in altering adsorbate states.

The pulsed laser deposition (PLD) technique has an upper edge over other conventional chemical synthesis methods for photo- and electrocatalytic applications. Depending upon the laser power, fluence, and other experimental conditions, it can provide the film with metal, metal–oxide, and alloy nanoparticle sizes under 10 nm. Figure 4.1(d) shows the green-colored plasma formation while fabricating the thin films, along with the optical and atomic force microscopy images showing the formation of nanoparticles with PLD [169]. Hence, we employed the PLD technique under vacuum conditions to create nanoparticulate thin films composed of the self-assembled CuO/Cu_2O interface, where this self-organization may be driven by the oxidation/reduction process of CuO in PLD, aiming to investigate the formation of Cu_2O at varying thickness levels. Our research delves into the plasmonic and photocatalytic properties of these CuO/Cu_2O thin films, explicitly focusing on understanding the mechanism behind hydrogen generation in relation to changes in band edges, nanoparticle size, and dimensions. To gain insights into the impact of thickness alterations on the role of plasmons, we utilized finite element modeling (FEM) simulations to analyze absorption curves. These simulations revealed distinct electric field distributions at the film surface and the CuO/Cu_2O interface. Furthermore, we explored the possibility of free electron presence at the interface through density functional theory simulations. In our experimental findings, we observed that in CuO/Cu_2O films with a thickness of ~ 13 nm and an average particle size of ~ 49 nm, light-matter interactions played a crucial role in hydrogen (H_2) generation. Our study demonstrates that plasmonic catalysis significantly enhances H_2 production, achieving a rate of $\sim 0.59\ \mathrm{kmolh^{-1}g^{-1}}$, provided that the dimensions, composition, and band alignment of the two interface materials are carefully selected. This self-assembled heterostructure design offers a promising strategy for harnessing hot electrons to enhance hydrogen production.

Section 4.3.1 delves into the theoretical detection of plasmons at the CuO/Cu_2O interface using finite element modeling (FEM) and density functional theory (DFT) simulations. It provides insights into transmittance, absorption, electronic structure, and permittivity spectra for the interface. To support this, we examine experimental evidence of plasmons using surface-enhanced Raman spectra (SERS) and an ellipsometer. In Sec. 4.3.2, we explore experimental hydrogen evolution reaction (HER) kinetics, focusing on adsorption and diffusion mechanisms before and after light fall. Section 4.3.3 comprehensively assesses the kinetics of HER. To conclude, we have discussed the mechanism of plasmonic catalysis with the thickness alteration using band alignment schemes and established benchmarks for reference.

4.2 Methods and Materials

4.2.1 Synthesis techniques

4.2.1.1 Bulk sample preparation

CuO (99%, Merck) powder was preheated at 300 °C for 1 h in a hot air oven. After grinding in pestle mortar at room temperature, it was passed through the sieve of 30 μm pore size. The preheated powder was then heated at 700 °C for 2 h. The heated powder was mixed with polyvinyl alcohol to form CuO pellets using a hydraulic press at a pressure of 5 tons. These pellets were further sintered at 700 °C for 2 h.

4.2.1.2 Thin film fabrication

CuO thin films were fabricated using the Pulsed Laser Deposition (PLD) technique [model COMPex 102 F with KrF excimer laser (248 nm)]. The target material is prepared by heating the CuO pellets sintered at 700 °C for 2 h in a conventional furnace. The pellet thus synthesized is taken as a target material and is mounted on the target holder. For deposition, the Si substrates of dimension 1 × 1 cm were ultrasonically cleaned with distilled water and acetone for 15 min each. Then, the substrates were heated at 100 °C for 30 min in a vacuum oven and mounted on the substrate holder for deposition. A laser beam of KrF Excimer laser (10 ns pulse width) is irradiated on the CuO target. The typical deposition process of the thin film is done in the vacuum (10^{-9} Torr) with 500, 1000, and 1500 laser shots on three different substrates (abbreviated as T5, T10, and T15, respectively). During ablation, the temperature of the deposition chamber is set to 200 °C, the frequency is set to 5 Hz, and the energy to 375 mJ.

The average thicknesses of the films obtained are 13, 22, and 27 nm for T5, T10, and T15, respectively.

4.2.2 Characterization

The structural characterization was done using BRUKER D8 ADVANCE ECO x-ray diffractometer with CuK_α radiation of wavelength (λ) 1.5405 Å in 2θ range from 20° to 80° at a scanning rate of 1°/min. The UV-visible absorbance spectra [using JASCO V-770 ultraviolet-visible (UV-VIS) spectrometer] of these thin films are recorded in the wavelength region of 200-900 nm. Atomic Force Microscopic (AFM) measurements are performed with contact tip, Golden Silicon probe tip CSG10/Pt at a resonance frequency of 140 kHz and force constant 0.01-0.5N/m. The automatic ellipsometer of Accurion, Park Systems GmbH, Germany, is used, and the spectroscopic ellipsometer was measured over the photon wavelength range from 200 to 1000 nm at room temperature. The angle of incidence was varied between 45° and 60°. Using the analysis reported in Ref. [170], optical constants n and k, along with ε' and ε'' have been calculated using spectroscopic ellipsometric angles Δ and ψ. The SERS measurement and Raman spectra using wavelength 532 nm are recorded using Witec Alpha 300 RAS, Germany. The electrochemical (cyclic voltammetry) measurements are performed by using a Keithley 2450 source meter with a three-electrode setup in a neutral medium using Pt electrodes as a counter electrode, Ag/AgCl as a reference electrode, and thin film samples as a working electrode. These measurements have been performed with the variation of the scan rate from 25 to 250 mV/s in dark and light (Keithley 2450 electrometer and Sciencetech solar simulator AAA class with AM1.5G filter). The chronoamperometric measurements are performed at constant potential (1.5 V) in dark and light for 4000 s. In order to find time, the current is fitted with an exponential decay equation. Here, the simulation is done for 400 iterations, and low-time currents are neglected. The open circuit potential, V_{OC}, was also studied using cyclic voltammetry in dark and light. The background correction has been applied to the cyclic voltammetry data. The reaction steps and Gibb's free energy of formation were determined using density functional theory simulations. The estimations of HOMO and LUMO were done with the empirical relation $E_{LUMO} = [(E_{red} - E_{1/2(ferrocene)} + 4.8)]$ eV or $E_{HOMO} = [(E_{ox} - E_{1/2(ferrocene)} + 4.8)]$ eV and $E_{1/2(ferrocene)} = 0.41$ V. The hydrogen production is studied in the form of a photoelectrochemical cell assuming 100% Faradaic efficiency, as illustrated in Fig. 4.19(inset). There are two general parameters to predict the hydrogen content, viz., turnover frequency (TOF in s^{-1}, H_2 (s^{-1})) and solar to hydrogen efficiency (STH, η_{STH}) measured as a function of current density are as follows:

$$H_2(s^{-1}) = j\,\frac{mA}{cm^2} \times \frac{1Cs^{-1}}{1000\ mA} \times \frac{1\ mol\ e^-}{F_cC} \times \frac{1\ mol\ H_2}{1\ mol\ e^-} \times \frac{N_AH_2}{1\ mol\ H_2} \quad (4.1)$$

$$\eta_{STH} = \frac{j \times 1.23(V)}{P_{in}\ (W/m^2)} \quad (4.2)$$

where Fc is the Faraday constant in Coulombs (C), NA is the Avogadro number, H_2 (s^{-1}), and η_{STH} estimated in the present case are compared with the literature [Figs. 4.20(a), Fig. 4.20(b) and Tables 4.3, Table 4.4 respectively].

The hydrogen production has been estimated as follows (in accordance with the literature):

$$Q\Delta V_s = \Delta E_{H_2}$$

$$\Delta V_s = \Delta H_{H_2/H_2O} + V_{OC}$$

Thus, the electric energy required for the production of 1 mol of H_2 is estimated in AVh (U_m),

$Q(C) = t \times$ area of catalytic curve in HER = $t \times \int J\, dV$.

$$\text{Thus, } H_2 \text{ produced} = \frac{\int J\, dV}{U_m} \times t \qquad (4.3)$$

4.2.3 Theoretical simulations

4.2.3.1 Finite element modeling (FEM) simulations

The finite element modeling (FEM) simulations (Comsol Multiphysics) were carried out using Floquet periodic boundary conditions and dielectric properties of Cu, CuO, and Cu_2O (optical permittivity, ε_∞ = 15.3, 7.1, and 9.3). We have used an incidence angle of 85.5° and roughness corresponding to the mesh size in the range of $4.5 \times 10^{-13} - 1.2 \times 10^{-10}$ m. The absorbance, transmittance, and reflectance S parameters (S_{21} for transmission and S_{11} for reflection) are estimated. The absorbance was derived using $1 - S_{21}^2 - S_{11}^2$ [171]. In order to find the absorbance, the interface has been applied with electromagnetic waves with quadratic electric field envelopes and fine triangular mesh,

$$(\nabla - i\nabla\phi_1) \times \mu_r^{-1}\left((\nabla - i\nabla\phi_1) \times E1\right) - k_0^2\left(\varepsilon_r - \frac{i\sigma}{\omega\varepsilon_0}\right)E1 = 0$$

$$\lambda = -i\beta - \delta_z$$

The wave equations applied at envelope 1 are

$$(\nabla - ik_1) \times \left((\nabla - ik_1) \times E1\right) - k_0^2\varepsilon_r E1 = 0$$

$$k_1 = \nabla\phi_1$$

For a perfect electric conductor, $\hat{n} \times \vec{E} = 0$, and boundary condition equations at the entry and exit port of the interface are $\hat{n} \times \nabla \times \vec{E} - j\beta\hat{n} \times \vec{E} \times \hat{n} = 0$. For the scattering parameters, scattering boundary conditions applied are $\hat{\mathrm{n}} \times \left(\nabla \times \vec{\mathrm{E}}\right) - (\mathrm{ik})\hat{\mathrm{n}} \times \left(\vec{\mathrm{E}} \times \hat{\mathrm{n}}\right) = -\hat{n} \times \left(\overrightarrow{E_0} \times ((ik)\hat{n} - ik_1)\right)e^{-ik_1.\vec{r}}$. Then, the field continuity equation is applied.

4.2.3.2 Density functional theory simulations

The calculations are carried out using the Hubbard model implemented in Quantum Espresso version 7.2 [172][173][174] as Dudarev's formulation [175]. First, the Hubbard, U, is optimized to match the bandgap and structural parameters with our experimental results. The LDA + U functional is used to describe the electronic states of strongly correlated systems and is done with a convergence value of 10^{-5} while varying U. We have performed self-consistent and non-self-consistent calculations for each U value to find the band structure that matches the experimental data. With the variation of U, the bandgap matches with the experimental value for U = 7.5 eV. A $(7 \times 10 \times 7)$ k-mesh is used for Brillouin-zone integration optimization of U calculations. Marzari–Vanderbilt–DeVita–Payne cold smearing is applied for all calculations. After the optimization of U, an interface is designed by combining the two phases, CuO and Cu_2O, as observed experimentally. Furthermore, we used a unit cell of CuO to design the interface. After that, the unit cell is transformed into a supercell $4 \times 4 \times 1$. Then, Cu_2O super cell $3 \times 3 \times 1$ is added in the X-Y direction from the plane (110). Then, the surfaces are reconstructed after removing the atoms from (110), (011), and (101) planes to form $\mathrm{Cu_{2-3x}O}$. The interface width is varied in the X and Y direction from 10 to 200 nm. Furthermore, alternate layers were relaxed in the interface for simulations, and then, the U value was optimized with thickness alteration. For a comparative, the U value was taken the same for CuO (optimized U where the theoretical bandgap matches the experimental one) and the interface. Then, the simulations were done in the 200 nm vacuum region in the X- and Z-direction in order to match the two structures. Furthermore, for the interface calculations, a $2 \times 2 \times 1$ k-mesh is used for Brillouin-zone integration to achieve the convergence value of 10^{-5}. However, the permittivity has been obtained using norm-conserving pseudo-potentials for the bulk and interface calculations. Furthermore, for the reaction steps simulations, the surface has been altered with adsorbed H, OH, H_2, and O_2 and find Gibb's free energy of formation for the adsorbate states. DFT simulations have also determined the equilibrium potential (~ 90 mV).

4.3 Results

4.3.1 Plasmonics at the CuO/Cu_2O

4.3.1.1 Theoretical assessment

Plasmons are collective oscillations of electrons in a material that can be excited by incident electromagnetic radiation, and its dispersion relation is subject to the Drude-Lorentz condition, i.e. [176],

$$\varepsilon(\omega) = \varepsilon(\infty) - \sum \frac{\omega_p^2}{\omega_0^2 - w^2 - i\gamma\omega} \tag{4.4}$$

where $\varepsilon(\omega)$ is the complex permittivity of the material as a function of angular frequency ω; $\varepsilon(\infty)$ is the optical permittivity of the material; ω_0 is the resonant frequency of the Lorentz oscillator, ω_p is the plasma frequency, which characterizes the collective oscillations of free electrons in the material; γ is the damping factor or linewidth of the Lorentz oscillator. The summation done for each possible Lorentz oscillation corresponds to the resonant modes of the materials. In the terahertz frequency regime, the compatible parameters to permittivity are transmittance (T), absorbance (A), and reflectance (R), which can be extracted from S-parameters (S_{11} and S_{21}) [177]. As for plasmonics, the effective permittivity must be negative, which should result in resonant absorbance with low reflection loss. For designing plasmonic devices, which can manipulate and control light at the nanoscale, the pre-idea of resonance behaviour is essential; therefore, here we consider configurations, i.e., C-1(CuO/Cu/CuO), C-2(Cu_2O/Cu/Cu_2O) (similar to Ref. [178]), and C-3(CuO/Cu_2O/CuO) with thickness of each slab 10 nm as shown in Fig. 4.2(a) insets, respectively, for which numerical simulations (FEM) are carried out (for details, please refer to Sec. 4.2.3). It can be observed that for all three configurations, S_{11} tip is below -15 dB, while S_{21} > 0 dB around incident light wavelength, λ ~ 1000 nm, suggesting the configurations are effectively transmitting or absorbing most of the incident radiation with minimal reflection. Interestingly, the S_{11} tip is the lowest for the C-3 configuration, i.e., S_{11} < -20 dB. Furthermore, the optical parameters, i.e., transmittance$(\mathrm{T} = \mathrm{S}_{21}^2)$, absorbance$(\mathrm{A} = 1 - \mathrm{S}_{21}^2 - \mathrm{S}_{11}^2)$, and reflectance $(\mathrm{R} = \mathrm{S}_{11}^2)$ are estimated from S-parameters, and their variations with wavelength are shown in Fig. 4.2(b). The sharpest absorbance maxima with reflectance minima are observed for the C-3 configuration, while it is wider for the C-1 and C-2 configurations. This increase in absorption shows that more photons are absorbed and interact with free electrons to form plasmon resonance, which is further associated with the electric field distribution, as shown in Fig. 4.2(c). Significant electric field enhancement is observed for the C-3 configuration, indicating a possibility of plasmon formation at the Cu_2O/CuO interface. It is necessary to mention that in the first two configurations, the metal-dielectric interface is considered, where the plasmonics phenomenon can occur due to Drude electrons from Cu (metal). Thus, our FEM simulation results are concomitant with the present understanding of plasmonics. However, the configuration C-3 possesses dielectric-dielectric interfaces where the presence of Drude (free) electrons is not obvious and, hence, plasmons. The origin of Drude electrons can be explained if and only if there exists a metallic phase at the CuO/Cu_2O interface to satisfy the Drude-Lorentz condition (see Eq. 4.4) as suggested by the FEM result. However, the FEM results only provide implicit understanding as it cannot predict the electronic states. In order to understand this behaviour explicitly, we need to understand the electronic states at the CuO/Cu_2O interface and, hence, perform DFT simulations (see subsection 4.2.3.2).

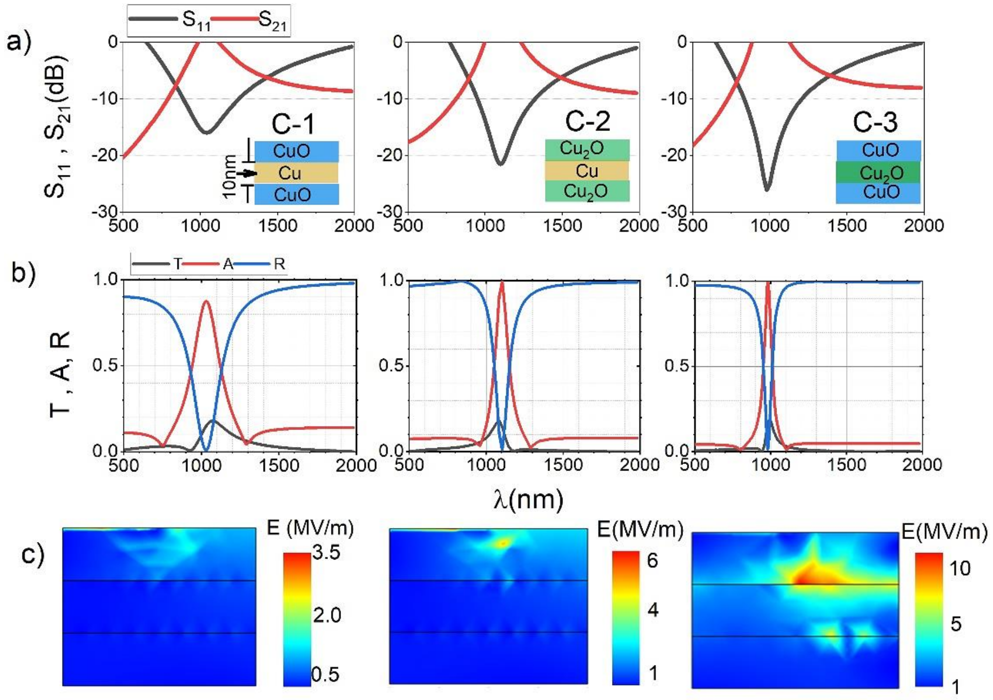

Figure. 4.2: (a) Variation of S_{11} and S_{21} (in dB) with wavelength for configurations, i.e., (C-1) CuO/Cu/CuO, (C-2) Cu_2O/Cu/Cu_2O, and (C-3) CuO/Cu_2O/CuO with thickness of each slab being 10 nm (illustrated, respectively, in insets). (b) Variation of transmittance (T), absorbance (A), and reflectance (R) is estimated from S-parameters; we can see that sharper absorbance is maximum with reflectance minima for C-3 configuration, satisfying the Drude-Lorentz condition for plasmonics to occur at the semiconductor interface supported by (c) significant electric field enhancement at the Cu_2O/CuO interface as compared to CuO/Cu and Cu_2O/Cu for 10 nm thickness (x-axis: $30 \times 30\ \mathrm{nm}^2$ and y-axis: $30 \times 30\ \mathrm{nm}^2$ are the dimensions of the layer).

CuO is monoclinic (C2/c) with lattice parameters 4.685, 3.426, and 5.130 Å, and Cu_2O is cubic ($Pn\bar{3}m$ symmetry) with lattice parameters 4.287 Å. The interface is prepared by merging the two phases, and here, we varied the interface width along the z-axis (Z_{if}), as shown in Fig.

4.3(a). It is observed in Fig. 4.3(b) that there is a continuous projected density of state (pDOS) with ~85% contribution of O (2p)↓ electrons and ~15% contribution of Cu(3d)↓ electrons around the fermi level for $Z_{if} \simeq 10$ nm. This strong p-d hybridization generates a metallic state in contrast to the bulk CuO semiconductor state, as shown in Fig. 4.3(b) (inset). This semiconductor state is in accordance with the theoretical result [179] and our experimental result [63]. In order to get the permittivity dispersion relation, we used norm-conserving pseudopotentials and plotted them in Fig. 4.3(c). It can be seen that the real part of permittivity is negative with plasmon energy 1.66 eV, satisfying the Drude-Lorentz relation explicitly. Also, the associated p-d interband transition is evident (loss peak in the vicinity of plasmon energy).

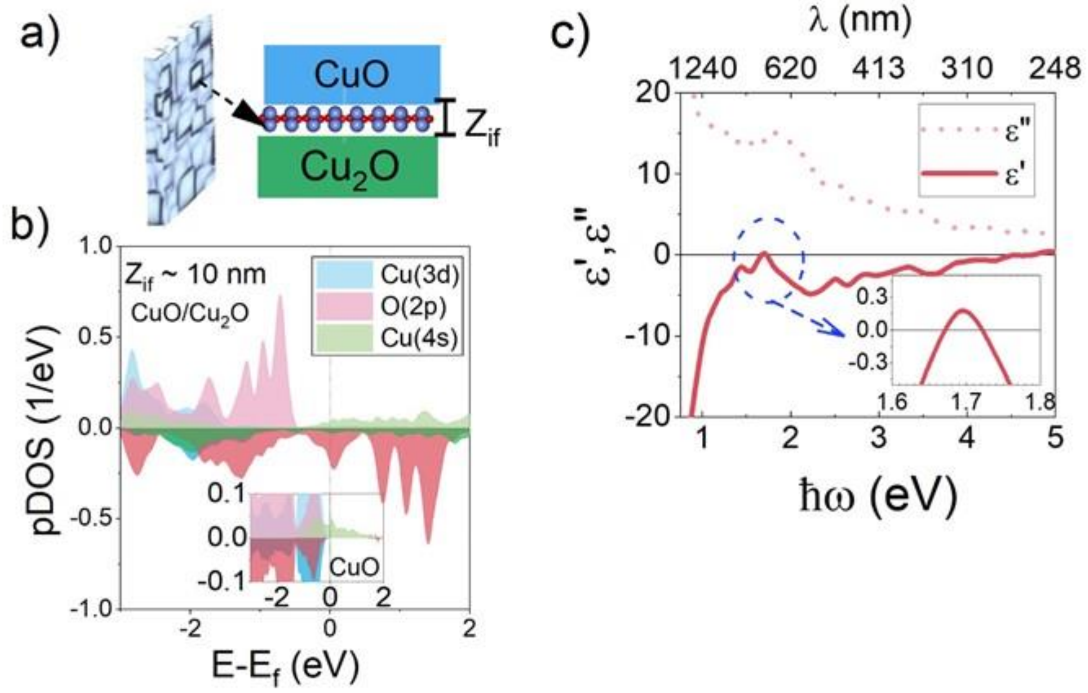

Figure. 4.3: (a) Interface structure of CuO (C2/c structure, blue horizontal layer) and Cu_2O ($Pn\bar{3}m$ structure, green horizontal layer) with thickness Z_{if}, (b) spin-polarized projected density of state (pDOS) for 10 nm thick interface; the inset shows pDOS for CuO, (c) permittivity dispersion curve: variation of real and imaginary permittivity for the 10 nm CuO/Cu_2O interface satisfying the Drude-Lorentz condition for plasmonics to occur at the semiconductor interface; the inset of (c) highlights the zoomed portion where the real part of permittivity changes its sign (negative to positive).

The inset of Fig. 4.3(c) highlights the zoomed portion where the real part of permittivity changes its sign (negative to positive). Therefore, plasmon generation at the CuO/Cu_2O dielectric interface is possible due to the evolution of the metallic phase at the interface, provided that the interface width is in the order of the monolayer.

4.3.1.2 Experimental verification

The average thickness of the film ($Z_f \simeq$ 13, 22, and 27 nm for T5, T10, and T15, respectively) as estimated from the peak height distribution-normalized frequency plot (for details, see Ref. [63]). Figure 4.4 shows a schematic view of Atomic Force Microscopy (AFM) image (left) with 2D optical microscopy image of thin films (right). It can be seen that the interface width is not homogeneous, i.e., different interface widths at different positions in all the films. The corresponding roughness and peak-to-peak height are tabulated in Table 4.1.

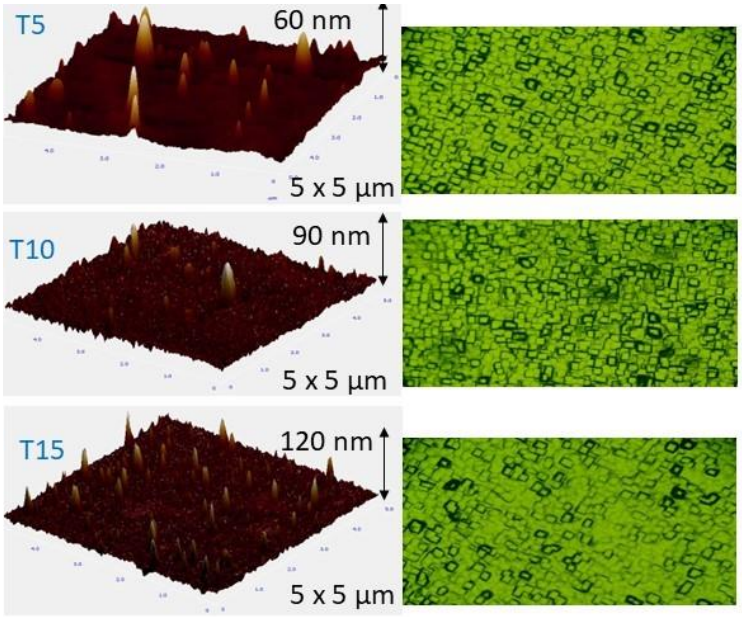

Figure 4.4: Schematic view of thin film formation: AFM image with 2D optical microscopy image (right) of thin film T5, T10, and T15.

In these thin films, particles have flat (2D) morphology with an average surface area size of ~ 49 nm, while thickness (height) is about 13 nm for T5. However, with an increase in the number of shots for T10 and T15, both average height (Z_f) and average areal particle size (mentioned in Table 4.1) increased as revealed by the particle size distribution curve as shown in Fig. 4.6(a), obtained from Atomic Force Microscopy (AFM) images. The inset Figure 4.6(a) shows the AFM image (1×1 μm) for T5. The AFM images (5×5 μm) used to generate the particle size distribution for T5, T10, and T15 are shown in Fig. 4.5, and the average particle size with the standard deviation for all the thin films is mentioned in Table 4.1. Figure 4.6(a) illustrates the formation of nanoparticles as the peak position is around 50 nm for all three thin films.

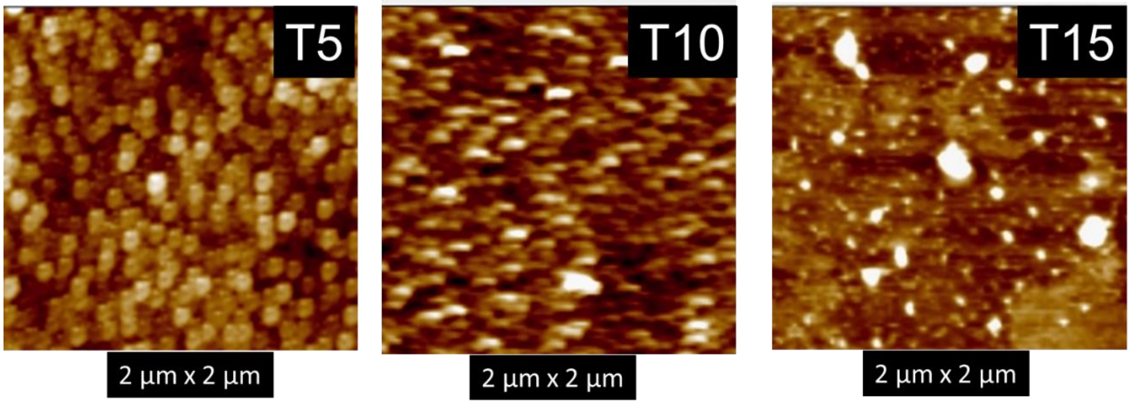

Figure 4.5: Schematic of AFM images showing the nanoparticle formation (with particle size variation) with the thickness variation.

To confirm the formation of plasmons in thin films, we conducted ellipsometric and Surface-Enhanced Raman Scattering (SERS) studies on the T5 sample. Surface plasmons are known to influence the real and imaginary components of the complex refractive index at the metal-dielectric interface. This, in turn, affects ellipsometric parameters, such as the ellipsometric angles (Ψ and Δ). These angles are highly sensitive to changes in the dielectric function, which is modulated by the presence of plasmons. Analyzing variations in the ellipsometric angles concerning incident angle, wavelength, or other parameters allows for identifying and characterizing surface plasmon resonances. These resonances correspond to specific conditions where incident light couples with surface plasmons and can be used to determine properties like the thickness of thin metal films, the dielectric constant of the surrounding medium, and the plasmon dispersion relationship. Also, Plasmons play a vital role in enhancing Raman scattering signals, enabling the detection and characterization of molecules at very low concentrations [167].

Fig. 4.6(b) presents the spectra of $\varepsilon'(\omega)$ and $\varepsilon''(\omega)$ for the T5 thin film measured by an ellipsometer. The figure reveals a distinct and sharp feature (absorption peak) at ~ 1.8 eV along with negative $\varepsilon'(\omega)$. Notably, the experimental results are consistent with simulated permittivity obtained via DFT and the broad peaks observed in Finite Element Method (FEM) simulations. It is worth mentioning that in prior ellipsometric data in the literature, $\varepsilon'(\omega)$ the curve for CuO did not exhibit such a sharp structure for pure CuO compared to sharp structures in the high-energy blue and indigo transitions for pure Cu_2O in bulk [170]. In this report, both CuO and Cu_2O are semiconductors and separately studied, and, therefore, positive $\varepsilon'(\omega)$ and $\varepsilon''(\omega)$ can be seen. However, our results are showing negative $\varepsilon'(\omega)$ due to the creation of the metallic interface, as elucidated in our DFT simulations.

In Fig. 4.6(c), an optical microscopy image depicts two interfaces where surface Raman spectra were recorded for the T5 sample. A white-colored interface, denoted by a black circle, represents the non-plasmonic interface, while the plasmonic interface is marked with an orange-black square.

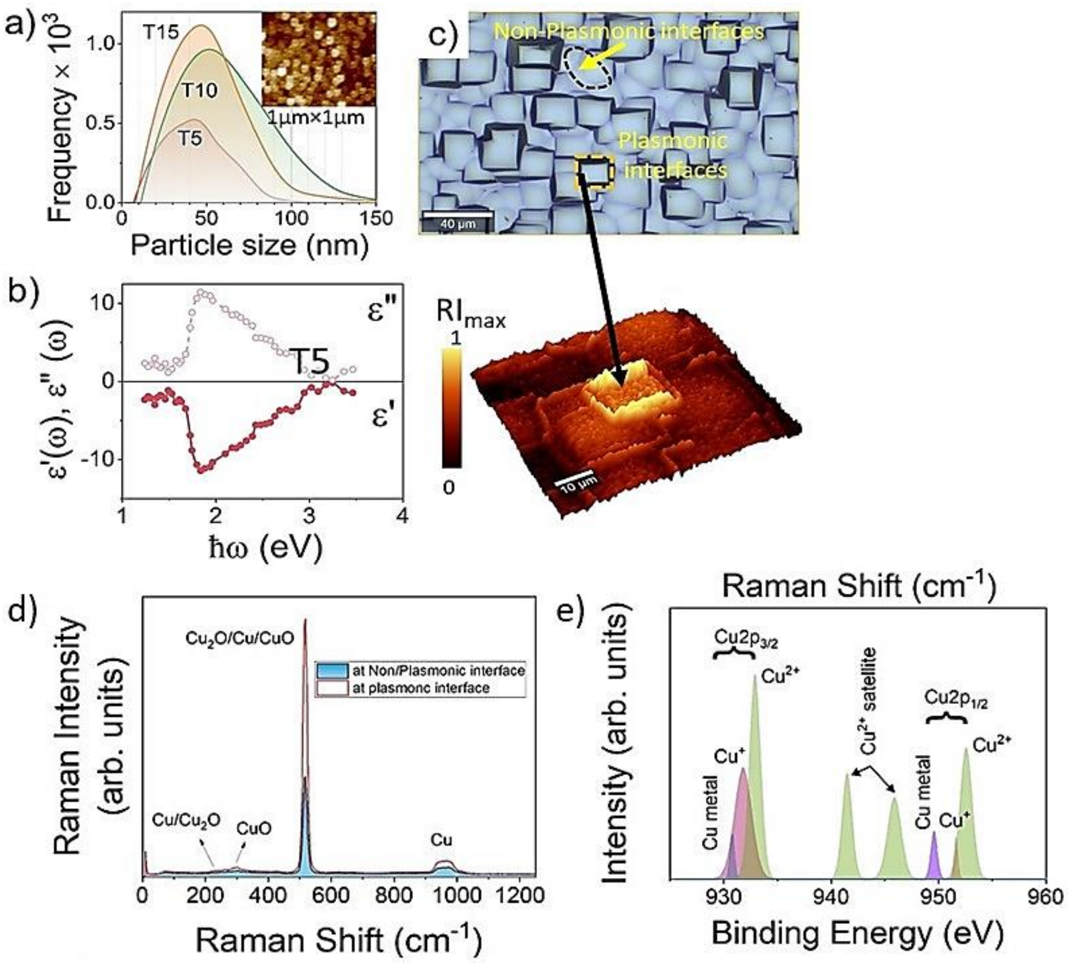

Figure 4.6: (a) Particle size distribution plots for the three thin films (inset) show the AFM image ($1 \times 1\ \mu m^2$) of T5. (b) $\varepsilon'(\omega)$ and $\varepsilon''(\omega)$ spectra of T5 thin film measured by an ellipsometer. (c) Optical microscopy image showing the two interfaces where Surface Enhanced Raman Scattering (SERS) is recorded for the T5 sample, a white colored interface shows the non-plasmonic interface (encircled in black), orange black square indicates the plasmonic interface, Raman imaging (at the bottom of optical microscopy shown by black arrow) at the orange black square interface shows the increase in normalized Raman intensity as compared to the white interface marked by the black circle. (d) Raman spectra at plasmonic and non-plasmonic centers for T5. (e) The deconvoluted XPS spectra in the binding energy range 920-960 eV for T5 thin films.

The number of plasmonic centers has reduced with the increase in thickness as shown in Fig. 4.5. Raman intensity (indicated by the Raman image at the bottom of the optical microscopy image, marked by the black arrow) is notably higher at the black square interface as compared to the white interface. Raman spectra showing the 2.5-fold increase in Raman intensity at plasmonic centers compared to non-plasmonic centers are observed for T5, as shown in Fig. 4.6(d).

Fig. 4.7(a) shows the SEM micrographs showing the square morphology (b) elemental content at different positions in SEM micrographs. The elemental content shown in Fig 4.7(b) indicates different Cu content at bulk and interface positions, which are congruent with Raman results showing plasmonic and non-plasmonic centers.

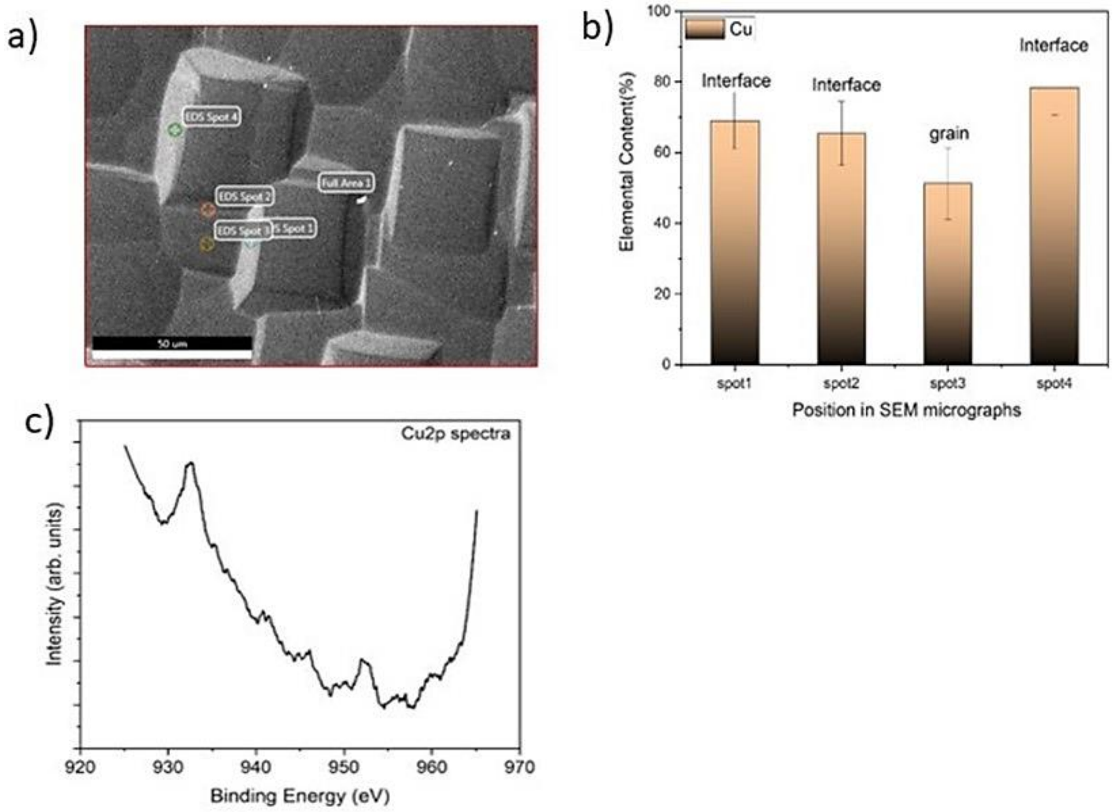

Figure 4.7: (a) SEM micrographs showing the square morphology, (b) Elemental content at different positions in SEM micrographs, (c) Raw XPS Cu2p spectra.

XRD analysis suggests that initially, along with CuO [monoclinic phase (C2/c)], the formation of Cu_2O [cubic ($Pn\bar{3}m$)] also occurs. The phase percentage of the Cu_2O phase formation with respect to CuO formation is tabulated in Table 4.1. It can be seen that in T5, the Cu_2O phase dominates. Furthermore, the Cu_2O phase reduces significantly with the increase in laser shots (for T15 ~ 0.10). Furthermore, it is well known that polarization modes are different for the different phases of Cu, viz., Cu, Cu_2O, and CuO [180][181].

Table 4.1 The photoelectrochemical parameters of bulk CuO and CuO/Si thin films at 300K.

Thin Films	**T0**	**T5**	**T10**	**T15**
Fabrication and z-dimension of thin films				
No. of shots	-	500	1000	1500
Z_f (nm)	-	13	22	27
Roughness (nm)	-	4	5	7
Average particle size (standard deviation) (nm)	-	49(18)	76(28)	60(24)
$\varphi_{Cu_2O}/\varphi_{CuO}$	-	2.20	0.58	0.10
Photoelectrochemical features				
E_g (eV)	1.4	1.65	1.61	1.52
V_{OC} (dark/light) (mV)	47/190	12/241	50/213	42/85
V_{FB} (dark/light) (V)	1.25/1.18	1.32/1.44	2.10/1.5	1.31/1.89

The peaks corresponding to the Raman shift in the Cu metal are observed at 214, 299, 512, 644, and 800 cm^{-1}. However, the peaks corresponding to CuO are observed at 298, 347, and 591 cm^{-1}, and Raman spectra of Cu_2O exhibit peaks at 218, 523, and 623 cm^{-1}. In the present case, we have observed the peaks corresponding to Cu multiple oxidation states as indexed in Fig. 4.6(d). Cu LMM spectra are recorded with Cu2p to detect chemical states, and the deconvoluted XPS spectra corresponding to Cu2p are shown in Fig. 4.6(e). The raw XPS spectra for Cu2p are shown in Fig. 4.7(c). It is observed that Cu2p spectra show spin-orbit splitting with Δ = 19.75eV. We have also observed Cu in all three possible states as Cu metal, Cu^+, and Cu^{2+} with the spin-orbit splitting. Furthermore, the satellite features can distinguish Cu oxidation states, and the collection of satellite features at ~ 942 eV confirms the Cu^{2+} state. It can also be seen that the intensities of the multiple oxidation peaks are in the order $Cu^{2+} > Cu^+ > Cu$. However, the peaks corresponding to Cu^{2+} are broader than Cu^+. In the present work, we have studied the cyclic voltammetry curves and estimated the parameters in the dark and under light exposure for photoelectrochemical cell applications.

4.3.2 Photo-electrochemical behaviour

Fig. 4.8 represents the cyclic voltammograms (CVs) in dark and continuous light exposure. The shape of CV curves is sigmoidal except for the thinnest film T5. In pure CuO, peak splitting disappears with the scan rate (for details with scan rate, see Fig. 4.9), and at 25 mV/s, $\Delta E_p > 180$ mV. Furthermore, during light exposure, peak current is observed only in the hydrogen evolution reaction (HER) regime, and no peak is observed in the oxygen evolution reaction (OER) regime. Moreover, hydrogen evolution is increasing with the increase in scan rate during light fall. In sample T10, the peak splitting is more prominent in the dark than in other studied samples.

The peak height and area under the curve are observed to increase with the increase in scan rate and $\Delta E_p > 180$ mV in both OER (marked downward arrows) and HER regimes. Interestingly, in Light, OER starts to reduce with an increase in scan rate (see the inset Fig. 4.8) as the peak diminishes in the OER regime, and no peak splitting is observed.

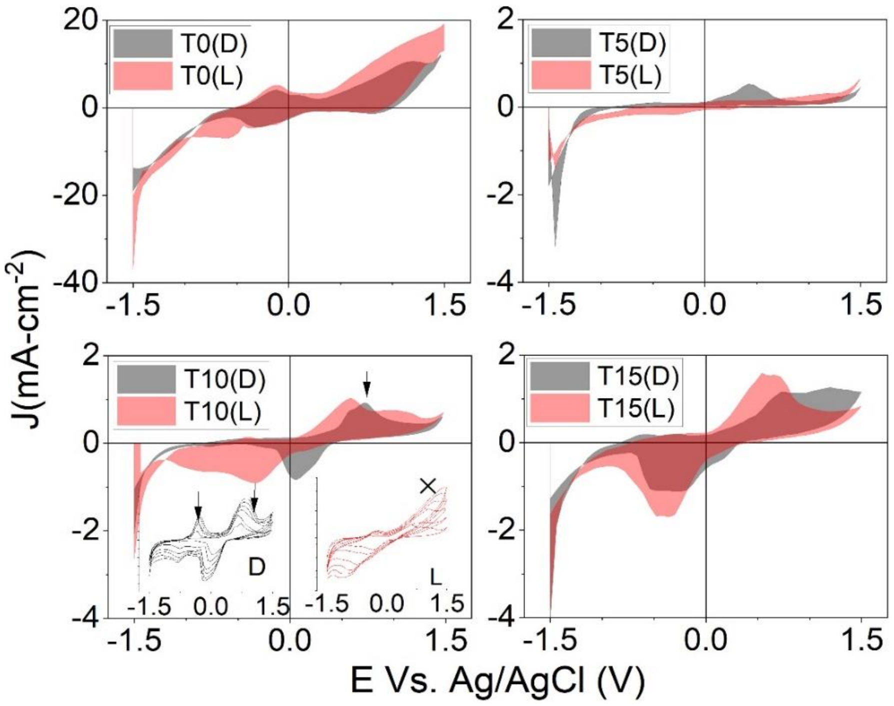

Figure 4.8: Cyclic voltammograms of bulk CuO and CuO/Si thin films in dark and continuous light exposure show a complex electrode reaction and electron transfer chain mechanisms (the inset of T10) show the voltammograms with the variation of scan rate in dark (black color) and under light exposure (red color), arrows in the inset indicate oxygen evolution reaction in dark, which is absent under light exposure and only hydrogen evolution takes place.

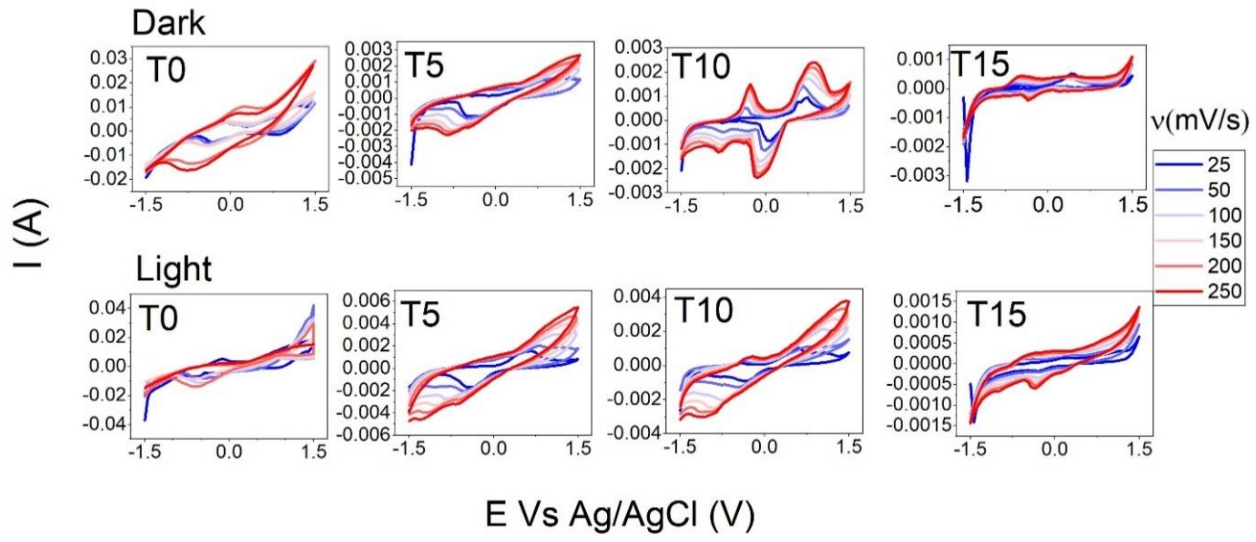

Figure 4.9: Schematic view of the voltammograms with the variation of scan rate in dark and under light exposure.

Meanwhile, the area under the peak is more in the HER regime than the OER regime. In the OER regime, almost similar behaviour is observed for the T15 thin film, whereas in HER, the peak splitting appears with scan rate, and with light exposure, it (peak splitting) increases to nearly three times. Even in T5, HER dominates over OER as the anodic current reduces and the cathodic current increases with the scan rate. However, in the dark condition, the potential difference corresponding to the anodic and cathodic peaks is ~ 57 mV, suggesting a complex electrode reaction mechanism [182]. However, in light, the peak splitting behaviour is again similar to other samples. In general, HER dominates over OER in these samples, with wide ΔE_p suggesting electron transfer chain mechanisms [84].

To quantify the effective role of nanostructures, we here introduce specific peak current density, $j_p^* \equiv j_p/m_a$ where j_p is the peak current density and m_a is mass of the active material. It can be seen that j_p^* increases with nanostructuring up to T10 and thereafter remains stable, irrespective of the change in thickness in dark as shown in Fig. 4.10(a). Moreover, during light exposure, current constantly increases from bulk to nanostructuring and then with the increase in thickness.

To find the number of electron transfers, the peak current is plotted vs $\nu^{1/2}$ to fit the Randles-Sevcik (RS) equation, as shown in Fig. 4.11(a). The plot is nearly linear for all the samples in the dark and with light exposure, suggesting the diffusion mechanism. In order to confirm the diffusion and adsorption-governed mechanism, the log-log plot of the scan rate with current density is shown in Fig. 4.11(b) and the slope lies between 0.5 and 1.0 for T0 and T5 as shown in Fig. 4.10(b) as compared to 0.2 and 0.4 for T10 and T15 in dark, suggesting major conduction through adsorption for T0 and T5 and major conduction through diffusion for T10 and T15 [84].

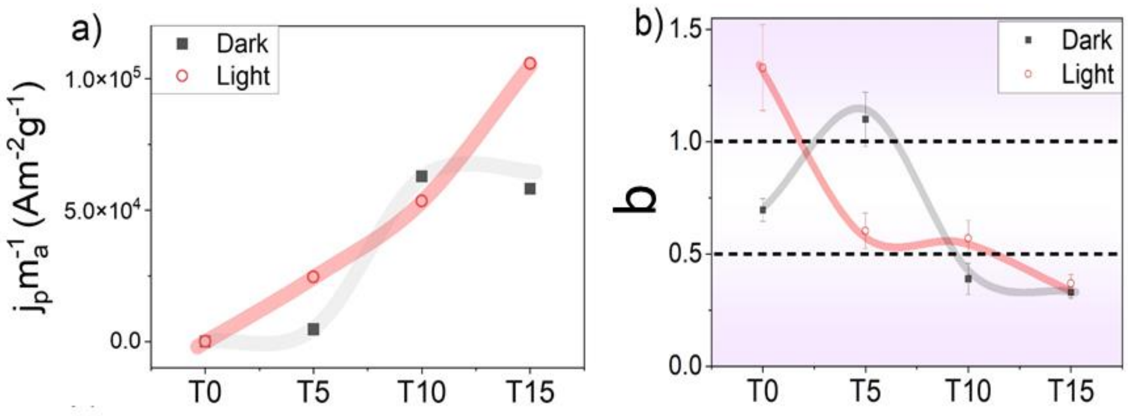

Figure 4.10: (a) Specific peak current density (j_p/m_a) showing that photocurrent density increases in thin film samples and is the highest in T15, whereas in the dark, specific peak current density saturates at T10 and (b) slope of log-log plot of the scan rate with current density for the T0 and three thin films, the white region indicates adsorption governed phenomenon corresponding to $0.5 \leq b \leq 1$.

However, under light exposure, the slope is greater than 0.5 up to T10, suggesting adsorption, and for T15, it is less than 0.5, suggesting diffusion.

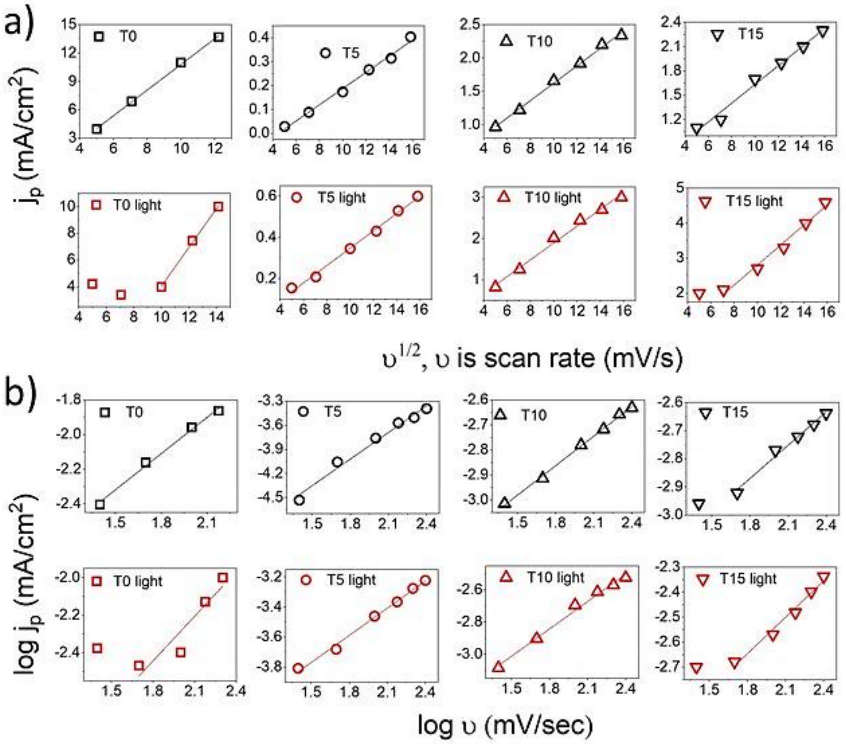

Figure 4.11: (a) Represents RS equation plot between the current density and $\upsilon^{1/2}$ for bulk and thin CuO (b) log-log plot of current density and υ for the studied samples.

4.3.2.1 Transient response at the interface

The transient current decay time is calculated by fitting the chronoamperometric response of bulk and thin films in the dark and during light exposure, as shown in Fig. 4.12. It is observed that during light fall, only T10 and T5 have the transient time of the order of 1 s. Meanwhile, T0 and T15 have transient times of 12 and 5 s, respectively, during light fall. However, all the samples have very high transient times in dark conditions. Thus, samples T5 and T10 are highly suitable for proton transport due to their less transient response during light fall.

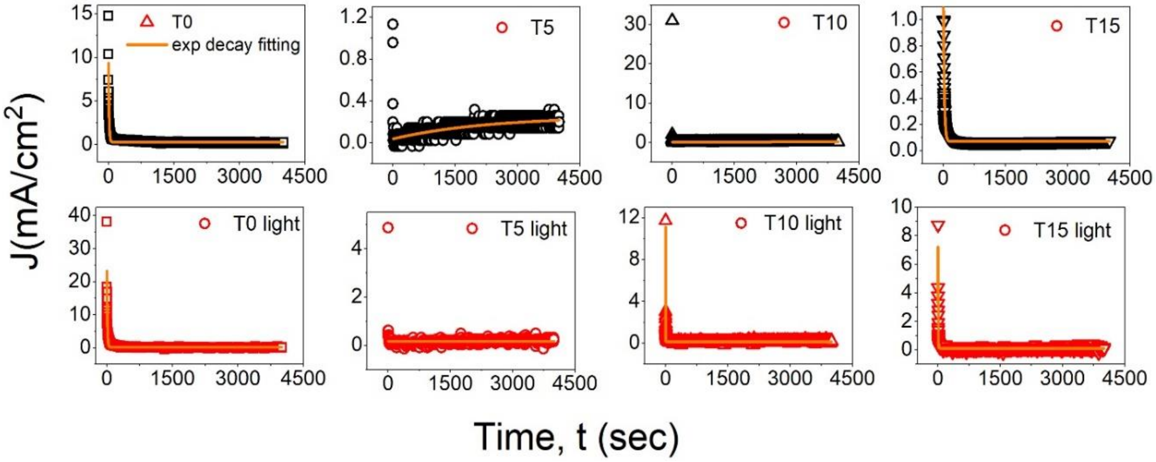

Figure 4.12: Represents chronoamperometric current density curve and time for the studied samples in dark and continuous light fall.

In order to verify the results of the RS equation, the number of charge transfer and diffusion coefficients are again estimated from the Shoup-Szabo relation [183], as shown in Fig. 4.13.

$$\mathrm{I} = \pi \mathrm{Fan_C cD}\left[1 + \left(\frac{\mathrm{P}}{\pi}\right)^{1/2} + 0.2732\ \exp\{-0.3911(\mathrm{P})^{1/2}\}\right] \tag{4.5}$$

$$\text{with } \mathrm{P} \equiv \frac{\mathrm{a}^2}{\mathrm{Dt}} \tag{4.6}$$

where I is the diffusion current, F is the Faraday constant, a is the radius of the disk electrode, n_C is the charge number of the electrode reaction, c is the concentration of the electroactive species, D is the diffusion coefficient, and t is the electrolysis time (see Fig. 4.10, J vs $t^{1/2}$).

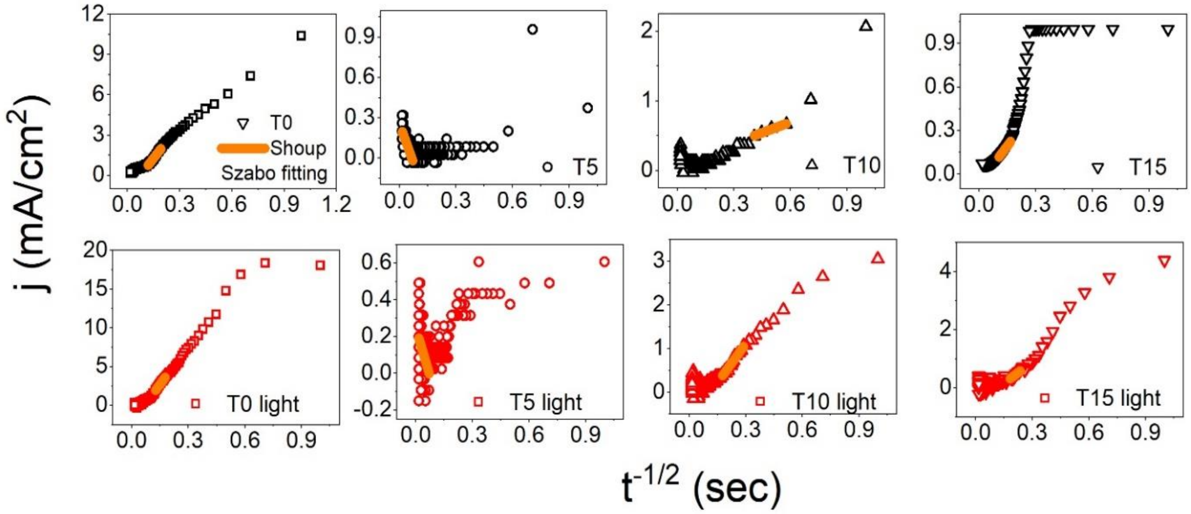

Figure 4.13: Represents Shoup-Szabo fitting for bulk and thin films in dark and continuous light fall.

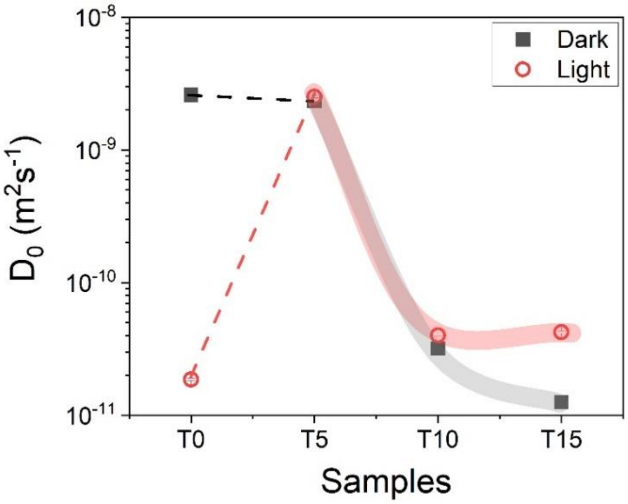

Figure 4.14: Variation of the diffusion coefficient in dark and under light exposure for all the studied samples and diffusion coefficient is unaltered in T5 before and after light exposure.

The estimated number of electron transfers is 6, 1, 3, and 2 for T0, T5, T10, and T15, respectively, in dark.

The estimated number of electron transfers is 1 for all the samples during light fall. The diffusion coefficient estimated is shown in Fig. 4.14. It can be seen that the diffusion coefficient for T5 is the same in dark and under continuous light exposure. With the increase in thickness, the diffusion coefficient increases with light exposure.

4.3.2.2 Interfacial capacitance

For the charge concentration and semiconductor nature, the Mott–Schottky relation is employed in the CV study [124][126]. It suggests that all the samples are p-type in the dark as well as under continuous light exposure (see Fig. 4.15).

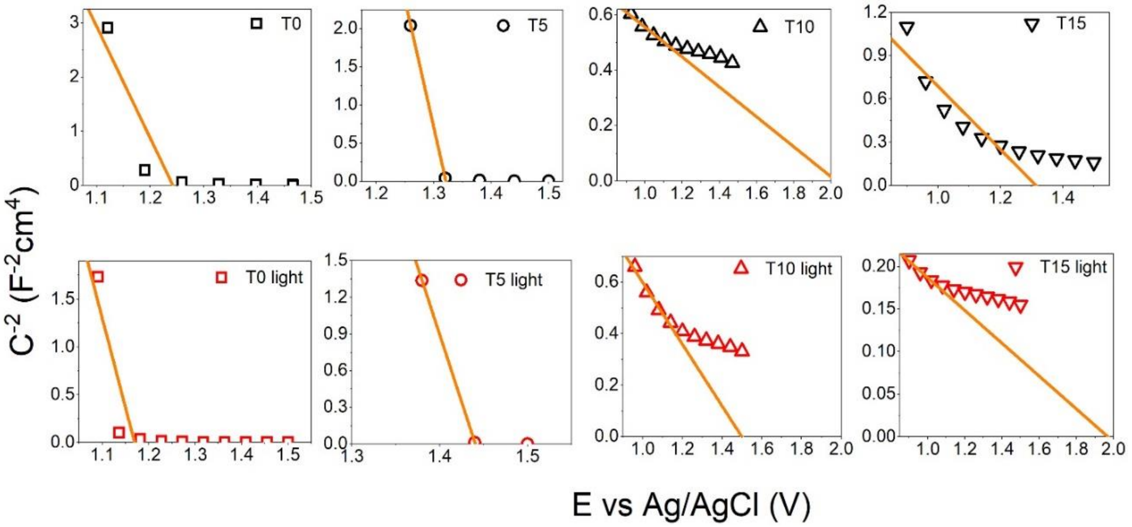

Figure 4.15: Mott-Schottky fitting for bulk and thin films in dark and continuous light fall.

The charge concentration estimated from the slope of Mott-Schottky plots showed that the charge concentration is nearly similar in T0, T5, and T10 in the dark as well as under continuous light exposure, as shown in Fig. 4.16(a). This is in correlation with the diffusion coefficient. Furthermore, there is an increase in the concentration of charge carriers from dark to continuous light exposure. The flat band potentials, V_{FB}, estimated from Mott–Schottky plots, are mentioned in Table 4.1. The specific capacitance is calculated using the relation ($C_{sp} = A/2\nu M_a \Delta V$) [184], where M_a is the active mass, and ν is the scan rate. The specific capacitance is nearly 800 Fg^{-1} for T15 under light exposure as compared to 500 Fg^{-1} in dark corresponding to 25 mV/s scan rate, respectively, as shown in Fig. 4.16(b). In order to illustrate the number of electron transfer, reaction pathways are suggested with the reduction potentials.

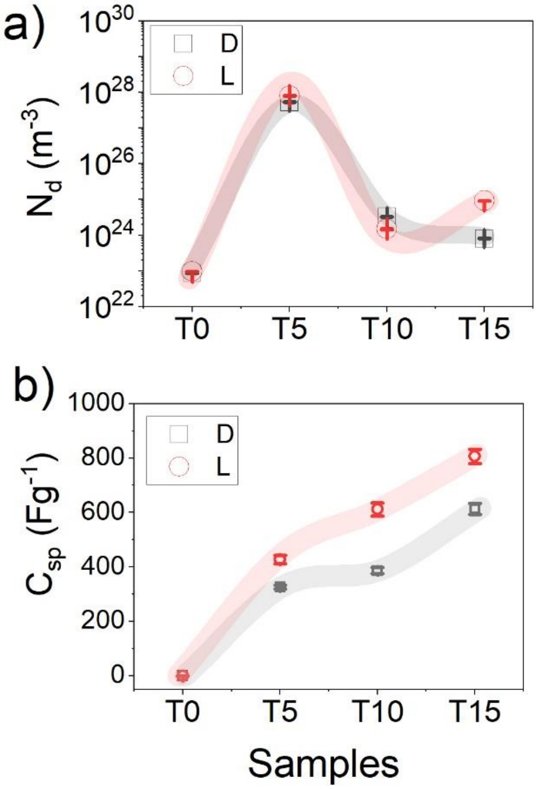

Figure 4.16: Mott-Schottky fitting for bulk and (a) Charge concentration is the highest in T5 and increases slightly with light fall and (b) specific capacitance in dark and under light exposure for all the studied samples.

4.3.3 Kinetics of HER

4.3.3.1 Reaction pathways

As estimated from the RS and Shoup-Szabo equations, the number of electron transfers varies in dark and light and is thus illustrated here. In the bulk sample, oxygen is adsorbed from the atmosphere at the triple-phase boundary and then leading to the formation of OH^- which further converts itself to O_2 and H_2 with the six-electron pathway. This is the reason for the oxygen generation in the bulk sample. This can be further confirmed through the Tafel slope in the later section.

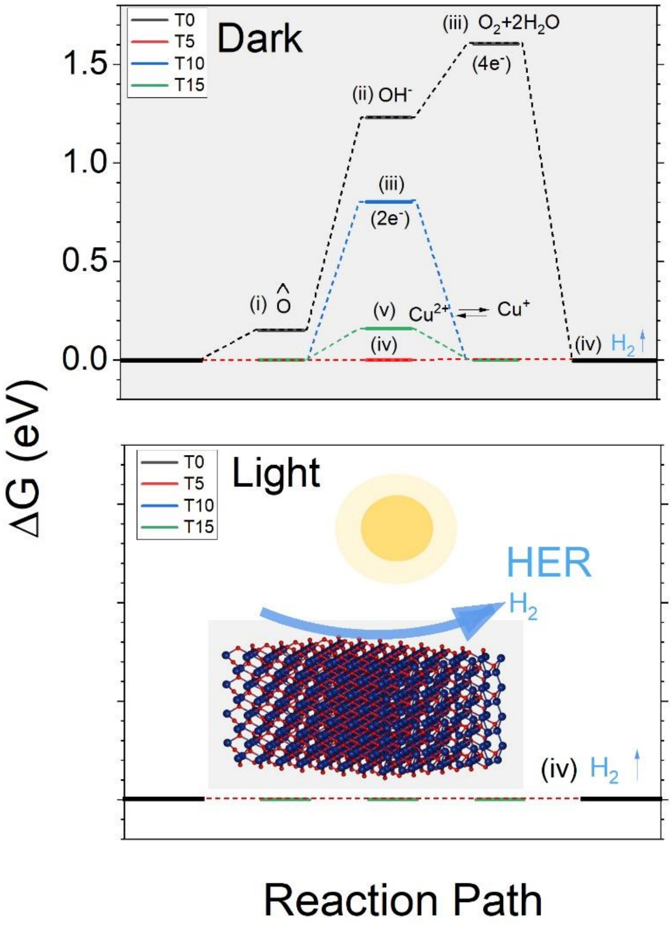

Figure 4.17: Free energy reaction pathway followed by the bulk system and thin films in dark and continuous light exposure. The Roman numerals are for reactions explained in the text.

Six electron pathways, as illustrated in Fig. 4.17, are as follows:

$$O_2 + \square \rightarrow 2\left(\frac{1}{2}\widehat{O}_2\right) \rightarrow 2\widehat{O} \tag{i}$$

Here, $\square$ is a vacancy and $\widehat{O}$ is adsorbed oxygen,

$$\widehat{O} + H^+ + e^- \rightarrow OH^- \tag{ii}$$

$$4OH^- \rightleftharpoons O_2 + 2H_2O + 4e^- \tag{iii}$$

$$H^+ + e^- \rightleftharpoons \frac{1}{2} H_2 \uparrow \tag{iv}$$

In thin film samples, CuO and Cu_2O formation is tabulated in Table 4.1. With the increase in thickness, CuO and Cu_2O formation varies, i.e., the content of Cu^{2+} and Cu^+ alters with thickness. In the sample where Cu_2O is high, one electron pathway is occurring with the direct formation of H_2,

$$H^+ + e^- \rightleftharpoons \frac{1}{2} H_2 \uparrow$$

Now, when CuO contents increase, a two-step pathway follows with the conversion of Cu^{2+} to Cu^+ and H^+ to H^2,

$$Cu^{2+} + e^- \rightleftharpoons Cu^+ \tag{v}$$

$$H^+ + e^- \rightleftharpoons \frac{1}{2} H_2 \uparrow$$

In sample T10, there is more oxygen evolution as compared to other samples. The three-step pathway is followed, where O_2 formation from OH^- takes place,

$$2OH^- \rightleftharpoons \frac{1}{2} O_2 \uparrow + H_2O + 2e^-$$

$$H^+ + e^- \rightleftharpoons \frac{1}{2} H_2 \uparrow$$

Under light exposure for all the samples, CuO reduces to Cu_2O with the liberation of O_2 and photoelectrons, one electron pathway is followed

$$2\mathrm{CuO} + h\nu \rightleftharpoons \mathrm{Cu_2O} + \frac{1}{2}\mathrm{O_2} \uparrow$$

$$\mathrm{H^+} + \mathrm{e^-} \rightleftharpoons \frac{1}{2}\,\mathrm{H_2} \uparrow$$

4.3.3.2 HER activity

The kinetics of the reaction can be explained in terms of the Butler–Volmer framework with the consideration of active mass M_a [182] as

$$j_s = (i_0/M_a) \sum C\, e^{\alpha\beta(E - E^0)}, \qquad i_0 = nFk_0 \tag{4.7}$$

where j_s is the specific current density, C is the surface charge concentration, k_0 is a reaction constant, n is the number of electron transfer, α is the charge transfer coefficient, and the thermal parameter $\beta = (k_B T)^{-1}$, and E^0 is the equilibrium constant.

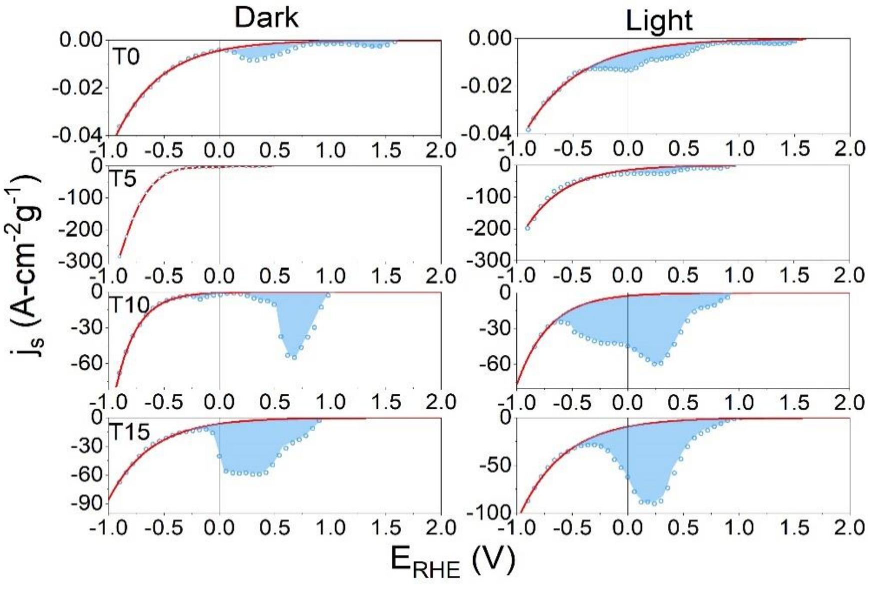

Figure 4.18: Cathodic js–E curves in dark and under light exposure revealing maximum area under the curve and H adsorption followed by H_2 generation.

The cathodic reaction curves are simulated with Eq. (4.7) as shown in Fig. 4.18, and deviation for the kinetic current curve is a measure of hydrogen evolution. The specific H_2 content, i.e., H_2/M_a is estimated to get attention toward the importance of nanostructuring; its ratio with the bulk sample is plotted in Fig. 4.19, and its distribution is shown in the inset. It is observed that in bulk CuO, ~ $\sim 8.07\ \mathrm{mmolh^{-1}}$ H_2 is liberated, while for thin films except T5 (where in the dark condition, H_2 liberation is relatively negligible $\sim 7.47\ \mathrm{mmolh^{-1}}$), a colossal increase (> 6000 times as compared to bulk) in the liberation of H_2 is obtained. Interestingly, in the T5 thin film [which is the thinnest as well as large in Cu_2O content ($\Phi \simeq 2.2$)] with light, a strong H_2 liberation is observed, as can be seen in Fig. 4.19(inset), which was almost absent in the dark. Thus, light-matter interaction plays a pivotal role in T5.

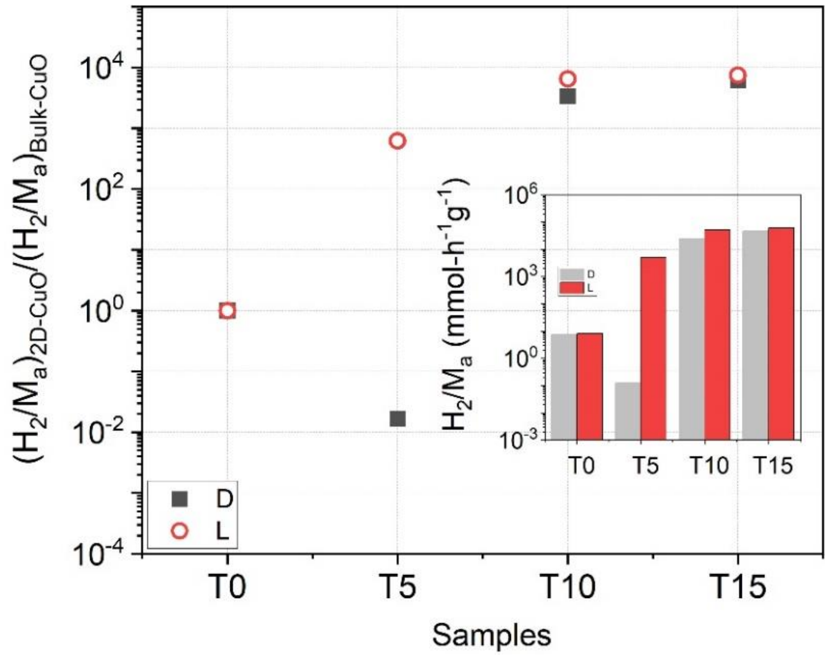

Figure 4.19: The specific H_2 content ratio for thin films and bulk samples in dark and under light exposure. The inset shows the specific H_2 content for thin films and bulk samples in the dark and under light exposure. The bulk sample had no change in H_2 content before or after light fall. A substantial increase in the H_2 content is observed in T5 after light fall.

The Tafel slope in mV/decade (β_{TS}) $\equiv \left(\ln(10) \times \frac{\partial \mathrm{E}}{\partial(\ln \mathrm{j})}\right)_{\mathrm{pH}}$ is an important parameter that reflects the reaction activity. To analyze the influence of light-matter interactions on the HER activity, we have estimated the cathodic Tafel slope ($\beta_{\mathrm{TS,\,C}}$ in mV/decade) with the thickness in dark and light (as shown in Fig. 4.20) after fitting the kinetic current-overpotential plot as shown in inset Fig. 4.20. The overpotential for HER activity has been taken as directly measured open circuit potential as mentioned [185], and a comparative of overpotential has been shown in Table 4.2 with the hydrogen electrocatalysts. It was observed that, $\beta_{\mathrm{TS,\,C}}$ decreases in all the samples with light exposure. In the dark, the estimated Tafel slopes $\beta_{\mathrm{TS,C}} \in \{40 - 55\}$ and while in light $\beta_{\mathrm{TS,C}} \approx 30$ for all the samples except for the thinnest sample, i.e., T5 ($\beta_{\mathrm{TS,C}} = 17$).

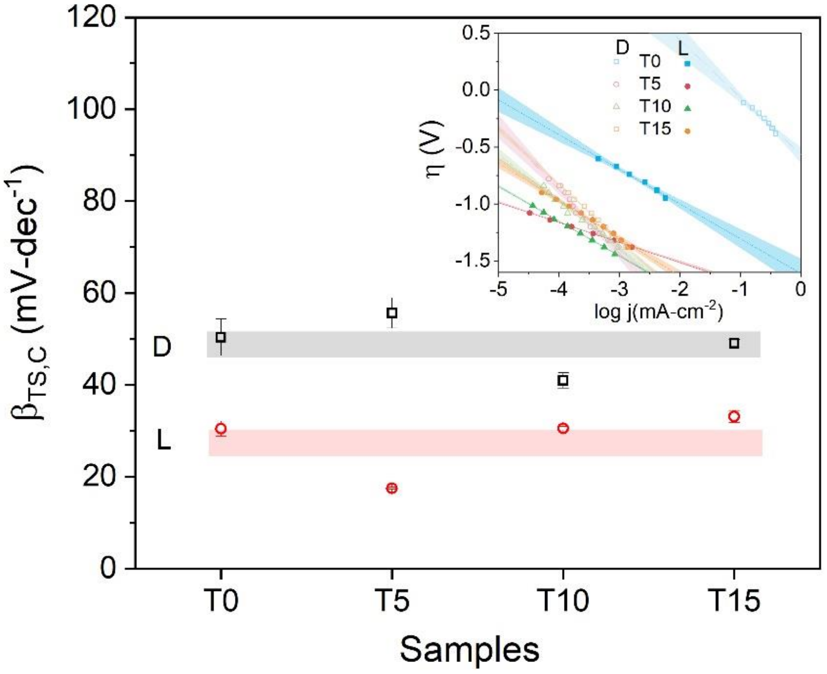

Figure 4.20: Variation of Tafel slope estimated suggesting high activity in samples after light fall and moderate activity in dark (inset) Tafel plot fitting (with 95% confidence band) for all the samples in dark and light.

It suggests better reaction activity using cyclic voltammetric study by creating multiple closer active sites with light interactions. However, in the dark, these active sites are distant from each other. As suggested by light interactions, $CuO \rightleftharpoons Cu_2O$ leading to O-O bond length reduction from 3.915(3) to 3.677(8) Å. Thus, copper site selectivity and content alteration upon light fall trigger the dissociation of adsorbed H, leading to more localized surface plasmon sites and plasmon generation.

Table 4.2 Bibliography for the Overpotential measured using the Tafel plot reported in these references.

Sample	Overpotential (mV) Acidic	Overpotential (mV) Basic	Overpotential (mV) Neutral	References
Ce-MOF	984	-	-	[186]
bulk Cu_2MoS_4	400	-	-	[186]
pristine TiB_2	848	-	-	[187]
TiB_2@PPy (6h)	432	-	-	[187]
$CoCl_2$	400	-	-	[188]
hexadecylpyridinium trichloro cobaltate	520	-	-	[188]
Co-N-doped carbon nanotubes	103	204	337	[189]
N,S-CNT		450		[190]
Ni_3S_2(55%)/ MWCNT		490		[191]
N-B/Carbon nanosheets	590	486	400	[192]
$NiWO_4$		750		[193]
WO_3/NPRGO phosphotungstic acid-polypyrrole/reduced graphene oxide	589			[194]
pure WO_3	660			[194]

rGO/CoP	599			[195]
GCE/RGO	700			[196]
NiTe/$NiTe_2$ nanosheets on C rod	422	679		[197]
Co-Cl_4-MOF	424			[198]
Co-Br_4-MOF	699			[198]
Nb electrode	78			[199]
Pt electrode	200			[200]
W electrode	400			[200]
Cadmium electrode	1150			[201]
lead electrode	1150			[201]
Ru electrode	899			[202]
Pt/C	35	200	300	[189]
Rh electrode	847			[202]
Mo	600			[203]
Pd	1500			[203]
Au	400			[203]
Ni wire		350		[204]
Fe, Co, or Ni-doped amorphous MoS_3			200-300	[205]
Metallic cobalt@cobalt-oxo/hydroxophosphate			385	[206]
T5			12	This work

4.3.4 Discussions

The maximum H_2 liberation is shown by sample T15 under light exposure, while light-matter interaction is prominent in T5, as discussed earlier. However, H_2 liberation (hydrogen adsorption) is related to the activity via Sabatier's principle. In addition to adsorption governed

Faraday conduction, electroactivity has one more crucial factor, i.e., e-electron occupancy in the case of transition metal cations. In transition metal cations, e-occupancy should be unity to felicitate hydrogen/oxygen evolution. Initially, to investigate electron transfer involving the 4s and 3d orbitals of Cu and the 2p orbital of O, considering the previously observed non-uniform interface width, we vary the thickness of the interface along the z-axis (Z_{if} (nm) ~ 200, 100, 50 and 10). Subsequently, we plot the partial density of states (pDOS) for both spin-up and spin-down states of Cu 3d, 4s, and O 2p orbitals, as depicted in Fig. 4.21. As explained earlier in Fig. 4.3(b) about the interface with Z_{if} ~ 10 nm, there is a continuous density of states. The zoomed portion in the inset Fig. 4.3(b) shows that there is a continuous projected density of states (pDOS) with ~ 0.1% contribution of $\mathrm{O(2p)}\downarrow$ electrons around Fermi level for $Z_{if} \simeq 50$ nm as compared to Z_{if} ~ 10 nm (a very small contribution from 4s). However, the contribution of O 2p electrons has further reduced with the increase in interface thickness, Zif > 100 nm, whereas the contribution of 4s electrons increases with a further increase in thickness. This metallic character is enhanced due to Cu 4s with increased $Z_{if} > 50$ nm. Therefore, all the interfaces with $Z_{if} < 100$nm should show collective excitation of surface plasmons. Furthermore, the non-monotonous behaviour of the calculated number of electron transfers and the diffusion coefficient with respect to film thickness could be attributed to the confinement of charge carriers within a limited volume. As shown in the DFT simulations of the interface, the interface is metallic, while the bulk sample is semiconducting. This alteration in electronic structure, density of states, and carrier transport properties has shown the change in the number of electron transfer from 6 to 1 in bulk and thin film, respectively.

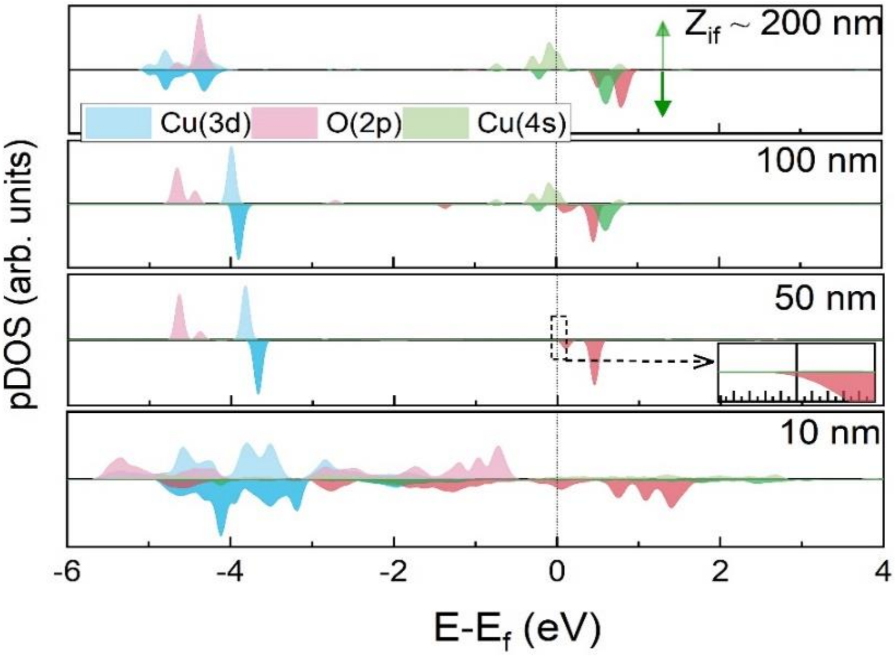

Figure 4.21: Variation of projected density of states (pDOS) for the spin-up and spin-down states of Cu 3d, 4s, and O 2p orbital (inset) shows the zoomed portion highlighted by a black square; there is a continuous projected density of states (pDOS) with ~ 0.1% contribution of O (2p)↓ electrons around the fermi level for $Z_{if} \simeq 50$ nm as compared to Z_{if} ~ 10 nm.

Furthermore, charge carriers could not be confined within a limited volume under the influence of light. In thin films (as observed experimentally), the bandgap widens by reducing film thickness ($Z_f < 100$ nm) is quite common due to quantum confinement, as evident here in T5, the thinnest film has the widest bandgap (Table 4.1). However, another important parameter emerged as a twist: the CuO/Cu_2O/CuO interface, width Z_{if} can generate plasmons provided $Z_{if} < 100$ nm. Though Z_{if} is not explicitly dependent on the thickness of films, nonhomogeneous Z_{if} is observed in all three films, but it depends on the relative content of Cu_2O, i.e., $\Phi \equiv \varphi_{Cu_2O}/\varphi_{CuO}$ (Table 4.1), which decreases with increased film thickness Z_f (more appropriately by number of shots). Therefore, with the increase in the thickness of the film, the number of plasmonic centers ($n(Z_{if})$) have reduced, i.e., $n(Z_{if}) \propto 1/Z_f$.

Furthermore, it suggests that $(\mathrm{n}(\mathrm{Z_{if}}))$, i.e., the plasmonic center content is more critical for the plasmon contribution toward plasmonic/photocatalysis.

Based on DFT simulations, we observed that the introduction of metallic properties in the thinnest film, T5, is accompanied by changes in the band diagram under both dark and light conditions, as demonstrated by experimentally observed HOMO and LUMO states (see Fig. 4.22).

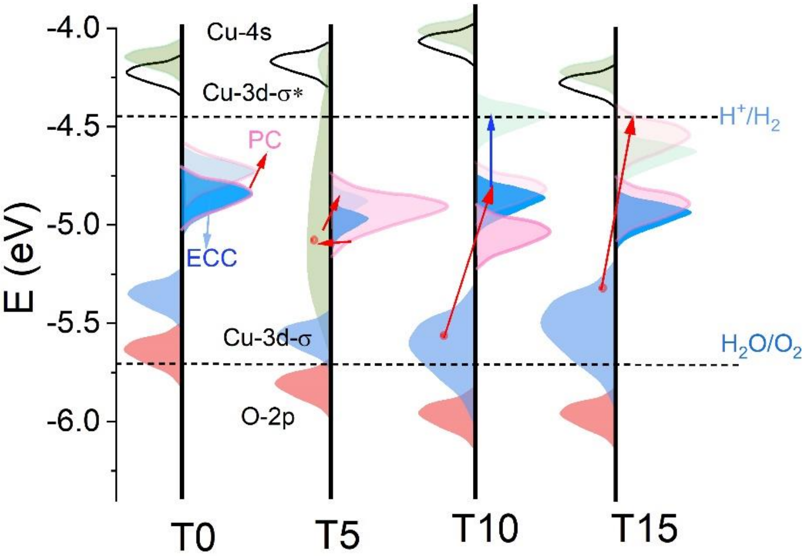

Figure 4.22: Illustration offers a plausible explanation for the experimental and theoretical observations. The equivalent positions of 3d-σ, 4s, and O-2p orbitals $(\mathrm{E} - \mathrm{E_f})$ position from Fig. 4.21 in the band diagram is estimated from DFT simulations, displayed to the left of the solid black vertical line. The red (light) and blue (dark) bands represent experimentally determined HOMO and LUMO positions, respectively, showcased to the right of the solid black vertical line. Blue arrows indicate ECC, while red arrows indicate PC.

Notably, this transformation facilitates the creation of various reaction intermediates and an extension of the σ^* band and 4s orbital (as observed in DFT simulations), which enhances the electron transfer between the 3d, 4s orbitals of Cu, and 2p orbitals of O in T5. Nevertheless, in thin films T10 and T15, the σ^* band and the 4s orbital of Cu engage in ECC, as illustrated in

Fig. 4.22. This indicates that the band alignment in the dark is adequate for H_2 production (as shown in Fig. 4.19, wherein there is minimal change in H_2 production following exposure to light). Consequently, light does not significantly influence H_2 production due to the reduced creation of plasmonic centers with increased particle size for T10 and T15 films. The band diagram illustrates that the HOMO/LUMO states in the T5 sample merge under both dark and light conditions, as depicted in Fig. 4.22. Conversely, in T10 and T15 samples, the HOMO/LUMO states are distinctly separated in both dark and light conditions. However, the LUMO state is situated close to the $\mathrm{H^+/H_2}$ conversion potential in the dark in T10. Additionally, it is worth noting that in T15, we observed that the LUMO state, in light, aligns precisely with the $\mathrm{H^+/H_2}$ conversion potential, resulting in an increased production of H_2. This observation suggests that in T5, indirect hot hole transfer from the HOMO to the valence band (VB) occurs, followed by Landau damping and the creation of the extended σ^* band, leading to the generation of plasmons. In contrast, in T10 and T15 samples, charge injection from the VB to the LUMO state is responsible for charge-induced desorption. Furthermore, the position of the band edge changes with a theoretical 59 mV voltage from Nernst's behaviour. As observed in the CV curves, there is a peak-to-peak separation of 57 and 180 mV or greater than that. Thus, altering the position of band edges ultimately boosts the solar to hydrogen conversion via plasmon decay along with electrochemical catalysis and gives a plausible mechanism for H_2 production difference observed in the thin films in dark and light (shown in Fig. 4.19).

4.3.5 Benchmarking

Fig. 4.23 compares the H_2 production with mass normalization of the electrocatalysts /heterostructures reported to date, along with the proposed self-assembled CuO/Cu_2O

interface. The graphitic carbon layered TiO_2 hybrid structures have liberated $3.046\ \mathrm{mmolh^{-1}g^{-1}}$ hydrogen [207]. C_3N_4 sheets/ZnS architectures $0.713\ \mathrm{mmolh^{-1}g^{-1}}$ as compared to pristine g-C_3N_4 [208]. With the creation of electron trap by S vacancies, composite nano heterostructure $\mathrm{MoS_2/ZnIn_2S_4}$ exhibited $6.884\ \mathrm{mmolh^{-1}g^{-1}}$ hydrogen evolution output, which is higher as compared to bulk $\mathrm{ZnIn_2S_4}$ [209].

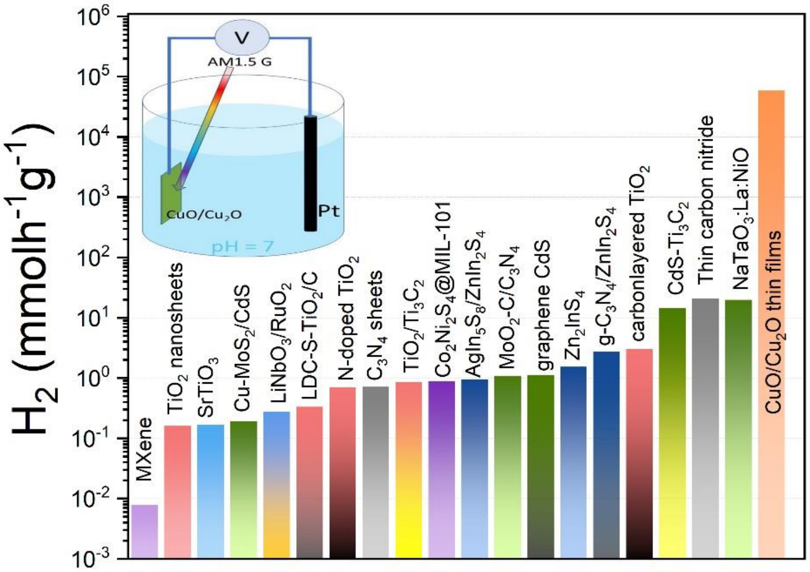

Figure 4.23: Comparative chart of H2 generation with mass normalization among various reported materials in recent times; the inset shows the schematic of a photoelectrochemical cell.

Various procedures, such as S impregnation, have increased the H_2 generation [210] but could not meet the level of chalcogenides. The thickness of bulk sheets of carbon nitride has been altered by Meng et al. to provide high active sites for surface reaction [211]. The morphology and heterostructure alteration created channels for charge separation in 2D/2D g-C_3N_4 nanosheet @$ZnIn_2S_4$ and showed $2.78\ \mathrm{mmolh^{-1}g^{-1}}$ H_2 production [212]. The core-shell microstructure of Au-doped anatase around a MOF core (MIL-101) enhanced visible light absorption, leading to the increment in the number of active surface sites has an impressive

$0.903\ \mathrm{mmolh^{-1}g^{-1}}$ H_2 production in water/methanol solution [213]. A 0D/2D heterostructure based on $\mathrm{AgIn_5S_8/ZnIn_2S_4}$ has shown increased active sites along with charge separation in comparison to their pristine samples and illustrated $949.9\ \mathrm{\mu molh^{-1}g^{-1}}$ H_2 production [214]. The CuO/TiO_2 interface has shown $64.2 - 71.6\ \mathrm{mmolh^{-1}g^{-1}}$ H_2 generation depends on the fabrication techniques [215]. Without mass normalization, a thin film with a thickness of 27 nm (T15) H_2 content liberated is $\sim 1129\ \mathrm{\mu molcm^{-2}g^{-1}}$ as compared to $240\ \mathrm{\mu molcm^{-2}g^{-1}}$ in photoelectrochemical cell/photovoltaic (PEC/PV) tandem cell $BiVO_4$:W, Mo/WO_3 as photoanode [216]. Our self-assembled photocathode has shown the outstanding $\sim 0.59\ \mathrm{kmolh^{-1}g^{-1}}$ H_2 production in CuO/Cu_2O film with thickness ~ 27 nm. Further, the turnover frequency (TOF) is estimated using the equation (4.1), and our best result is compared to other reported catalysts, as shown in Fig. 4.24(a) in Table 4.3. Remarkably high solar to hydrogen efficiency (η_{STH}) of ~ 12.2% is estimated using the equation (4.2), as shown in Fig 4.24(b), and compared with other photoelectrodes in Table 4.4.

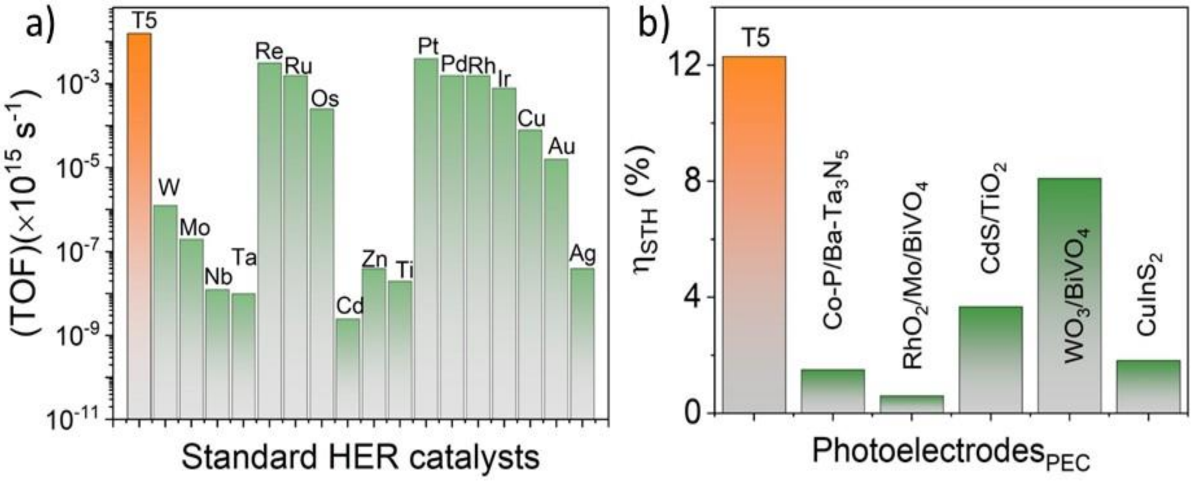

Figure 4.24: (a) Turnover frequency (TOF) calculated using the current densities reported and compared with the present work. (b) Solar to hydrogen efficiency (η_{STH}) reported for photoelectrodes in photoelectrochemical cell (PEC) applications and compared with the present work.

Table 4.3 Bibliography for the Turnover frequency calculated using the current densities reported in these references

Standard HER Catalysts	References
W	[201]
Mo	[203]
Nb	[217]
Ta	[217]
Re	[218]
Ru	[219]
Os	[220]
Cd	[201]
Zn	[221]
Ti	[222]
Pt	[200]
Pd	[203]
Rh	[201]
Ir	[221]
Cu	[221]
Au	[221]
Ag	[223]

Table 4.4 Bibliography for solar to hydrogen efficiency (η_{STH}) reported for photoelectrodes in photoelectrochemical cell (PEC) applications

Photoelectrodes	References
Co-P/Ba-Ta_3N_5	[224]
RhO_2/Mo/$BiVO_4$	[225]
CdS/TiO_2	[226]
WO_3/$BiVO_4$	[227]
$CuInS_2$	[228]

4.4 Conclusion

In the present study, light exposure eliminated the effect of Cu_2O defect in the CuO crystal as the whole reaction mechanism occurred by one electron transfer process. Compared to dark conditions, the charge transfer occurred via 6, 1, 3, and 2 electrons, respectively, for T0, T5, T10, and T15. This suggested the maximum H_2 liberation $\sim 0.59\ \mathrm{kmolh^{-1}g^{-1}}$ H_2 production in the CuO/Cu_2O film with thickness ~ 27 nm under light exposure. However, the light-matter interaction has played a crucial role in ~ 13 (±5) nm (with an average particle size of < 50 nm), where light fall has shown a drastic increase in H_2 production. This is correlated with the increase in adsorbed charge carriers under light exposure with the interband merging of s, $\mathrm{d} - \sigma^*$, and p-orbital. This is in correlation with the simulation studies, which suggest the different electric field distributions around the CuO/Cu_2O interface. Thus, band edge merging in ~ 13 (±5) nm thin film with Cu_2O/CuO content ~ 2.2 ultimately boosted the solar to hydrogen conversion via plasmon decay. The self-assembled heterostructure design of CuO/Cu_2O by the PLD technique provides a strategy to exploit hot electrons in order to convert light into energetic electrons. This work provides a promising perspective for maximum H_2 generation in water electrolysis as a cost-effective photocathode for photoelectrochemical cell applications. It is well known that CuO/Cu_2O composition variation is inherent during CuO thin film fabrication. Nevertheless, a comprehensive exploration of the stoichiometric variations, structural reconstructions, and charge transfer dynamics occurring at the interface between the two oxide materials is imperative to understand their interfacial properties thoroughly.